

Signature of Indian Ocean Dipole on the western boundary current of the Bay of Bengal

Sherin V Raju^(a,c), Fabien Durand^(b), Gopalkrishna V. V.^(a,c), Anuvinda S.^(a,c), Chaitanya A V S^(a,c), R. Bourdallé-Badie^(d), F. Papa^(b,c).

revised version submitted to Deep Sea Research I
March 2nd, 2018

(a) NIO-CSIR, Dona Paula, Goa, India

(b) Laboratoire d'Etudes en Géophysique et Océanographie Spatiales (LEGOS), UMR5566, Université de Toulouse, CNES, CNRS, IRD, Toulouse, France

(c) Indo-French Cell for Water Sciences (IFCWS), IRD-IISc-NIO-IITM Joint International Laboratory, Bangalore 560012, India

(d) MERCATOR Ocean, Parc Technologique du Canal, Ramonville Saint Agne, France

Abstract

This study uses an unprecedented collection of 27 years of repeated Expendable Bathy Thermograph (XBT) sections crossing the western and north-western boundaries of the Bay of Bengal (BoB). Our objective is to analyse the variability of the boundary current that flows there, known as the East India Coastal Current (EICC). In the western BoB, in line with the past observational and modelling studies, our dataset confirms that the EICC seasonally flows poleward from February to July (with a peak transport of 5 Sv), then decays and reverses to equatorward towards the equator from October to December (with a peak transport of 3 Sv), reversing again to poleward in December. In the north-western BoB, the seasonal EICC prominently flows north-eastward, with a peak transport of 7 Sv in March. Over the rest of the climatological year, the transport remains north-westward and weak (of order 2 Sv at most). Beyond the seasonal climatology, the time span of our dataset allows us to put a special emphasis on the departures from the seasonal cycle of the EICC velocity and transport. It is observed that this non-seasonal variability is actually larger than the seasonal climatology, so that the seasonal cycle may be completely distorted in any given year. This is true in the western boundary region as well as further offshore in the central BoB and concerns the surface as well as the subsurface layers. Indian Ocean Dipole (IOD) events influence EICC variability, supposedly through remote forcing from the equatorial Indian Ocean and generate northward (southward) anomalous transport typically reaching 5 Sv (7 Sv) in winter during positive (negative) IOD events. In addition to IOD events, most of the variability observed at inter-annual timescales seems to be driven by ocean turbulence. A comparison of our observed current with a suite of state-of-the-art ocean reanalyses and model products (SODA, ORAS4, MERCATOR-ORCA12) confirms this hypothesis, with non-eddy resolving models overestimating the wind-driven IOD influence on EICC variability. Our results emphasise the benefit of a sustained long-term monitoring programme of the EICC, spanning the entire continental slope region up to its offshore edge, associated with a modelling approach that would be capable of accounting for the oceanic turbulence, to decipher the various processes forcing the variability of the western boundary current (WBC) of the Bay of Bengal and their inter-play.

Keywords: Bay of Bengal, monsoon currents, EICC, IOD

1. Introduction

The Bay of Bengal (BoB) is the north-eastern part of the Indian Ocean (Fig. 1). Landlocked on the north, this bay is characterised by seasonally reversing monsoonal winds. It receives a heavy fresh water influx due to both large river runoff and intense precipitation, altogether exceeding the basin-scale average evaporation. The upper BoB circulation is marked by its WBC called the East India Coastal Current (EICC)(Schott and McCreary, 2001). The current reverses direction twice a year under the influence of the reversing monsoon winds (McCreary et al., 1996; Shankar et al., 1996). It plays a keyrole in the exchange of water masses between the Arabian Sea (AS) and the BoB (e.g., Shetye et al., 1996; Vinayachandran et al., 1999; Jensen, 2001; Shankar et al., 2002; Durand et al., 2007; Akhil et al., 2014, 2016; Benschila et al., 2014).

Seasonally, the EICC flows poleward from February to September, with a peak flow during April and May, and equatorward from October to January, with a peak flow during November (Laurindo et al., 2017; Mukherjee et al., 2014). Although this reversal is intimately linked with the reversal of monsoonal winds over the Indian Ocean, the mechanism is complex and involves a combination of remote and local forcings. The current during the summer monsoon and pre-summer monsoon seasons is attributed to local alongshore winds and Ekman pumping in the interior BoB(Shetye et al., 1991, 1993). The remote forcing from the Equatorial Indian Ocean (EIO) was shown to influence the circulation of the Bay of Bengal (Potemra et al., 1991; Yu et al., 1991). The wind variability over the EIO triggers equatorial Kelvin waves, which reflect on the coast of Sumatra, generating coastal Kelvin waves there, which propagate along the periphery of the BoB, eventually reaching its western boundary (McCreary et al, 1993). Using a linear model, McCreary et al. (1996) and Shankar et al. (1996) systematically analysed the four linear forcing mechanisms of the EICC, namely, local along-shore winds, Ekman pumping in the interior of the bay, remote forcing from the northern and eastern boundaries of the bay and remote forcing from the EIO. They could conclude that the seasonal cycle of the EICC is the result of these various forcing mechanisms, each of which being significant at one time or another during the seasonal cycle.

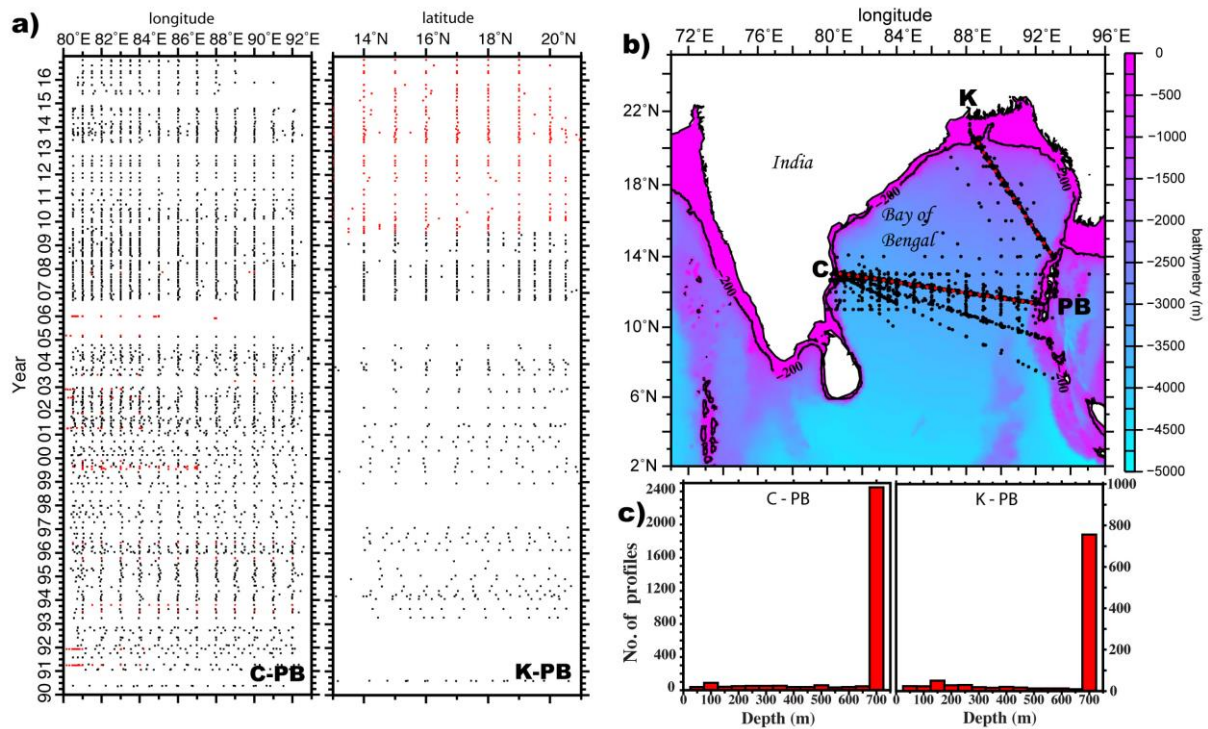


Figure 1. (a) Space-time data distribution along the Chennai (C) - Port Blair (PB) transect (left), and along the Kolkata (K) - Port Blair transect (middle). Black dots indicate XBT casts, red dots indicate CTD and XCTD casts. (b) Spatial distribution of the entire set of profiles (black dots); the red dots feature C-PB and K-PB mean tracks, as defined in the text. The shade represents the ocean bathymetry (200 m isobath in solid black). (c) Distribution of the depth of *in situ* profiles used in this study, for the (left) C-PB route and the (right) K-PB route.

The deviations of the EICC from its seasonal climatology are comparatively less understood due to the limited observational data available in the region. At interannual time scales, variability of the winds in the equatorial region and in the BoB influences the sea level and circulation of the Bay (Han and Webster, 2002). The Indian Ocean Dipole (IOD), a climatic phenomenon that has two phases (positive and negative), exhibits anomalous wind patterns over the equator (Saji et al., 1999; Webster et al., 1999). Using an ocean model, Rao et al. (2002) showed that during a positive IOD event, an upwelling Kelvin wave propagates along the periphery of the BoB, which results in an anti-cyclonic anomalous circulation. Also based on numerical models, Thompson et al. (2006) and Jensen et al. (2007) reported similar anomalous anticyclonic circulation in the BoB during the post-monsoon of a positive IOD. Vice-versa, during a negative phase of the IOD, the winter climatological cyclonic circulation pattern is enhanced. In the course of the past decade, the advent of spaceborne coastal altimetry revealed the turbulent character of the EICC along its pathway. Durand et al. (2009), using a specific altimetry dataset, demonstrated a discontinuous EICC from north to south,

forming recirculation loops that were highly variable at intraseasonal as well as interannual timescales.

The intraseasonal and interannual variability of the EICC was found to be essentially decorrelated along its path. Mukherjee et al. (2014) used a four-year record of moored current-meters all along the Indian coastline, the first of its kind in the region, to document the variability of the EICC at different time scales. They observed a strong seasonal cycle with considerable variability at intraseasonal and interannual timescales, also decorrelated along the coast. In addition to the IOD, the El Niño-Southern Oscillation (ENSO) is known to influence the BoB circulation at interannual timescales (Srinivas et al., 2005; Jensen, 2007). Though the IOD and ENSO leave distinct signatures in the sea level anomaly in the Bay (Aparna et al., 2012), few studies suggest that the impact of the IOD in the BoB circulation variability is much higher than that of the ENSO (Rao et al., 2002; Rao et al., 2010; Currie et al., 2013; Pant et al., 2015).

The EICC is an important piece of the Asian climate system. As the BoB receives an excess freshwater supply, it has to export this water mass out of the basin. The EICC ensures most of this export (Benshila et al., 2014; Chaitanya et al., 2014). A large fraction of it is transferred to the Arabian Sea. This water mass exchange plays an important role in the regional climate as it influences the vertical stratification of the two sub-basins (e.g., Chaitanya et al., 2015), which in turn has the potential to impact the basin-scale heat budget and thus the monsoon dynamics (Shenoi et al., 1999, 2002). As a result, any modulation of the EICC transport (such as during an IOD event) may have climatic consequences. Beyond its climatic implications, EICC variability is also known to affect the biological productivity of the BoB (Madhupratap et al. 2003; Currie et al., 2013).

Despite the knowledge gained over the past two decades, studies on the western boundary of the BoB suffer from a lack of observational coverage compared to other tropical western boundary current systems. The abovementioned descriptions have been based either on coarse ship-drift data (Laurindo et al., 2017), episodic hydrological cruises (Shetye et al., 1991, 1993, 1996; Wijesekera et al., 2015), surface-only satellite data (Durand et al., 2009), or point-wise current-meter moorings records (Mukherjee et al., 2014). A description based on long-term, sustained, high-resolution observations encompassing the cross-shore as well as vertical extent of the EICC, capable of resolving the temporal spectrum of variability from seasonal to inter-annual timescales, is still lacking. In addition to observations, we have seen that the scientific community has relied heavily on ocean circulation models to analyse EICC structure and variability. However, it turns out that EICC characteristics are strongly model-

dependent (e.g., Benschila et al. 2014). This is particularly true for the subsurface part, where the limited amount of observations does not allow us to assess or fine-tune the current generation of numerical models. Currently, the limited data availability results in a tendency to rely on state-of-the-art ocean reanalyses for studies in this region (e.g., Wijesekera et al., 2015; Jensen et al., 2016; Chowdary et al., 2016). However, the quality of these integrated datasets remains largely unknown. For example, comparisons with ADCP data show that ECCO2 and GODAS poorly reproduce the EICC (Mukherjee et al., 2014).

The motivation of the present study is to investigate the characteristics of the EICC that can be observed from an original 27-year-long record of XBT/XCTD sections that transect the EICC in the western BoB (along 13°N) and in the north-western BoB (approximately 19°N). The pluri-decadal time span is unprecedented and allows a robust analysis of the interannual variability of the EICC. This said, it must be noted that our dataset allows a depiction only of the geostrophic part of the flow, whereas the western boundary currents are known to be significantly influenced by ageostrophic dynamics. To shed light on the validity of state-of-the-art numerical products, we compare our observed features with three model data sets, namely, SODA, ORAS4 and MERCATOR ORCA12, which differ in resolution (from non-eddy to eddy-resolving) and in modelling strategy (with/without data assimilation). In Section 2, the *in situ* dataset, numerical products and methodologies are presented. The structure of the EICC that is observed and modelled in the western BoB is provided in Section 3. In Section 4, we analyse the influence of the Indian Ocean Dipole on the interannual variability of the EICC. Section 5 is devoted to the EICC flowing in the north-western BoB. Section 6 concludes the study.

2. Data and methods

2.1 XBT/XCTD dataset

We use an unprecedented dataset of repeated XBT sections that were operated from passenger ships plying between the India mainland and Andaman Islands in the BoB, spanning the 1990-2016 time-period. A data record with such a timespan is unique in this part of the world ocean. The sections cover two different transects from Chennai to Port Blair (henceforth C–PB) and from Kolkata to Port Blair (K–PB). Both transects run roughly perpendicular to the western boundary of the basin, at 13°N and 20°N, respectively (Figure 1). Data are usually collected at monthly frequency (one-way cruises), with typically 10 deployments per transect. This amounts to a typical spatial resolution of 1° along both transects, with enhanced resolution (approximately 0.5°) in the coastal part of both transects. Overall, we achieved 211 cruises along C–PB, and 123 cruises along K–PB. As shown in

Figure 1, we faced a nearly 2-year-long temporary interruption of data collection in 2005-2006 because of funding contingencies during this period. Apart from that, no major gaps exist in our data record. Sippican manufactured XBT T7 probes (0.1°C sensor accuracy) are used for deployments. The fall rate equation used is based on Hanawa et al. (1995). The XBT data are processed and quality controlled according to the standard procedures described in Bailey et al. (1994). Each profile is visually verified for consistency and to identify outliers such as sharp abnormal spikes. To adjust for the thermal response of the thermistor of the XBT probes, the temperature measured at 4.5m is applied upward up to the surface. Along the K–PB transect, from May 2009 onwards, XCTD probes were used instead of XBT probes. These are TSK manufactured XCTD–1 probes (0.02°C for temperature and ± 0.03 mS/cm conductivity accuracy). The quality control is the same as that followed for XBT probes. After the above quality control process, a total of 2886 XBT profiles along the C–PB transect and 720/363 XBT/XCTD profiles along the K–PB transect are used for our analysis. Most profiles reach 700m depth (Figure 1c).

2.2 CTD dataset

We also considered Conductivity-Temperature-Depth (CTD) profiles (Seabird device, temperature sensor accuracy 0.002°C, salinity accuracy 0.002 PSU) collected onboard various research vessels during hydrographic cruises along the C-PB route. A total of 16 such cruises were made available to us by the National Institute of Oceanography Data Centre (NIO DC) of India. These CTD profiles are shown as red dots in Fig. 1a. Each profile was quality controlled using standard Seabird software. Abnormal salinity biases were checked by comparison with the temperature-salinity relationship developed from the Northern Indian Ocean Atlas (NIOA) climatology of Chatterjee et al. (2012). Overall, 192 such CTD profiles are used in this study.

2.3 Geostrophic current computation methodology

The dataset was spatially gridded cruise by cruise through a running average over 1° bins. This step is meant to smooth out the signature of high-frequency ageostrophic features such as internal tides, which are ubiquitous in our profiles (not shown). We operated this gridding on a 0.5° regular grid along the C–PB and K–PB nominal tracks, shown as red dots in Fig. 1b. Given the relatively high and uniform spatial coverage of our *in situ* profiles, we preferred this simple method to a more sophisticated analysis scheme such as optimal interpolation or kriging. Our method is similar to that used by Taft and Kessler (1991). The tracks extend from 80.5°E to 92.5°E for C–PB and from 14°N to 20.5°N for K–PB. For the

few transects when data gaps exist, the filling was done by linear interpolation of the neighbouring profiles. We computed the monthly climatology of temperature for the two sections, from the surface to 700 m. The comparison with NIOA climatology for the same region revealed a consistent, slightly warm bias (of order 0.3-0.5°C typically over the upper 150m). This small bias is commensurate with the typical uncertainty of state-of-the-art climatologies over the study area. We fixed the 700-m depth as the level of no motion in our computation of geostrophic currents. Wherever the XBT gridded profiles are shallower than 700m, we simply fill the gaps with our XBT monthly climatology.

Using climatological temperature and salinity data from the NIOA, T–S relationships are developed for each grid point for each month. From this, we infer a synthetic salinity profile for each of our XBT temperature profiles. Of course, CTD and XCTD casts provide temperature and salinity profiles that we used directly. Density ρ is then generated using this temperature and salinity profiles, following the Jackett et al. (2006) equation of state. Cross-track geostrophic currents are calculated using the thermal wind equation:

$$V = \frac{g}{f\rho} \frac{\partial}{\partial x} \int_{-h}^0 \rho(z) dz$$

where the spatial derivative is computed by centered finite difference between pairs of neighbouring grid points, along each track. The vertical integral is computed from 700m to the surface. Hence, vertical current profiles are generated every 0.5° from 80.75°E to 91.75°E (C-PB route) and from 14.75°E to 20.25°E (K-PB route). This implies that our dataset encompasses the deep region of the coastal ocean, and essentially leaves the slope and shelf regions out of the field-of-view for both transects. Finally, the resulting currents were horizontally filtered using a 1° low-pass Hanning filter, leaving the first two grid points (nearest to the coast) untouched.

2.4 Ocean reanalyses

As we said in the introduction, we assessed two state-of-the-art-ocean reanalysis products in comparison with our observational dataset to quantify their capability to capture the western boundary current of the BoB. We first considered the European Centre for Medium-range Weather Forecasts (ECMWF) Ocean Reanalysis System 4 (henceforth ORAS4) (Balmaseda et al., 2013). ORAS4 uses version 3.0 of the NEMO ocean model (Madec, 2008) with an ORCA1 grid. ORCA1 is a global grid with 1° resolution and refined meridional resolution in the tropics reaching 0.3° at the equator. The model has 42 vertical

levels, of which 18 levels are in the upper 200m. The model assimilates temperature and salinity profiles as well as along-track satellite-derived sea-level anomalies. Temperature and salinity profiles are obtained from XBTs, CTDs, TAO/TRITON/PIRATA/RAMA moorings and Argo profilers. The sea-level anomaly data are provided by AVISO (Archiving, Validation and Interpretation of Satellite Oceanographic data). The model is forced by daily atmospheric heat and freshwater fluxes taken from ERA-Interim reanalysis (Dee et al., 2011) from January 1989 to December 2009, and from ECMWF operational analysis from January 2010 onward. The model is also relaxed to climatological salinity and temperature values of World Ocean Atlas (Zweng et al., 2013; Locarnini et al., 2013). Because this reanalysis was only available through 12/2014, we considered the 1990-2014 period. We checked that all results presented hereafter are not sensitive to this slight mismatch with our observational period (1990-2015).

We also used version 2.2.4 of Simple Ocean Data Assimilation (henceforth SODA) (Carton and Giese, 2008). SODA uses version 2.1 of the Parallel Ocean Program (POP) ocean general circulation model (Smith et al. 1992), with an average $0.25^\circ \times 0.4^\circ$ horizontal resolution and 40 vertical levels with 10-m resolution near the surface. The model assimilates salinity and temperature profiles obtained from World Ocean Database (Boyer et al., 2013). The model is forced by wind stress from Twentieth Century Reanalysis version 2 (C20Rv2; Compo et al., 2011) and heat fluxes derived from bulk formulae. SODA is available until 12/2010. Thus, we considered the maximal common period with our observations, 1990-2010. We also checked that our subsequent analyses and conclusions are quantitatively insensitive to this mismatch with our observational period. Temperature and salinity profiles from the reanalysis products are bilinearly interpolated along the C-PB and K-PB tracks. Then, cross-track geostrophic currents are computed similarly to those of the observations.

2.5 NEMO ORCA12 model

Aside from the reanalysis products mentioned above, we also used a free (i.e., non-assimilating), eddy-resolving simulation of the NEMO (Madec, 2008) model based on version 3.5 of the code and implemented on an ORCA12 global grid (Hewitt et al., 2016). This grid has a $1/12^\circ$ horizontal resolution. It is used in the Mercator-Ocean operational system to perform 10-day forecasts (Lellouche et al., 2016). The present experiment uses 75 vertical levels (with 31 levels in the upper 200 m). This simulation is forced by ERA-Interim (Dee et al., 2011) momentum, heat and freshwater fluxes and covers the 1979-2015 period. Similar to the two reanalysis products, we checked that the subsequent results reported in this paper are

insensitive to the slight mismatch with our observational period (2016 being unavailable in ORCA12 simulation). The parameterisation used for the dynamics includes a quadratic bottom friction, and a vertical mixing scheme based on GLS scheme (Umlauf and Burchard, 2003) in a k-epsilon version of the turbulence closure. No tidal forcing is applied. The side wall boundary condition on the along-shore flow allows a free slip. This parameterisation of the boundary frictional layer was indeed found critical to enable a realistic transport of the EICC in a regional version of ORCA12 (Benshila et al., 2014). The model run is hereafter referred to as ORCA12. Similar to the ocean reanalyses, ORCA12 geostrophic current is computed from temperature and salinity profiles that are bilinearly interpolated to the ships tracks.

3. Chennai–PortBlair transect

3.1 Seasonal climatology

Figure 2 presents the longitude-depth sections of the monthly climatology of the current obtained from our *insitu* observations along the C–PB transect. It is apparent that the strongest and most variable flow is trapped against the western boundary (typically between 81°E and 83°E). Generally, the flow is intensified in the upper 200m. The boundary current (referred to as EICC) flows northward in February, and increases in March–April. It remains northward (though of lesser magnitude) until August. By September, the boundary flow almost disintegrates, giving way to an equatorward flow in October, which peaks during November and decays in December. The core of the boundary current spans the upper 200m when it flows poleward, whereas it appears shallower (down to 100m or so) during its equatorward phase in November. The climatology agrees well with the known patterns reported from past observational studies (see e.g., Laurindo et al., 2017; Durand et al., 2009; Mukherjee et al., 2014). On the offshore flank of the boundary current, a counter current is often observed (in March, June, July, August, November, December), suggesting the presence of recirculation cells, as already reported by Shetye et al. (1996) and Durand et al. (2009). In general, just like the boundary current, those counter currents are also trapped in the upper 150m.

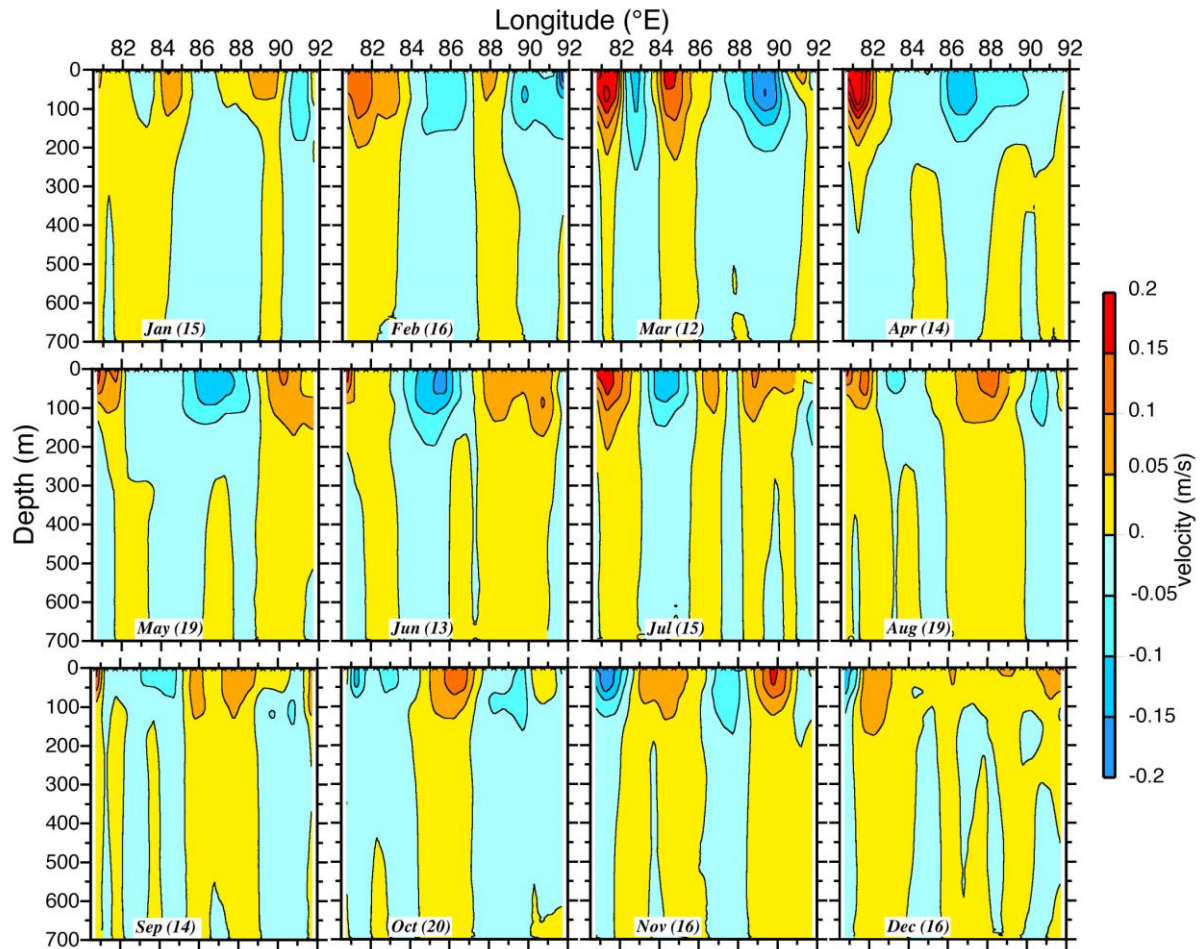


Figure 2. Monthly climatology of observed cross-track geostrophic current along C-PB route. The number of individual cruises used to compute each month climatology is indicated between brackets. Positive values indicate northward flow. The contour interval is 0.05 m/s.

As a preliminary assessment of the three ocean models we considered, Figure 3 shows selected months of their current climatology along the C-PB. We chose these particular months to highlight the distinct phases of the observed EICC evolution, with February (establishment of the northward flow), July (summer peak northward flow) and November (peak equatorward flow). Mostly, all three numerical products successfully capture the reversal of the boundary current from northward (February) to southward (November), but with clear differences. ORAS4, for instance, seriously underestimates the northward-flowing EICC in July. In February, SODA overestimates the flow velocity in the EICC core (at 81°E, throughout the 0-300m layer). Offshore, the alternating bands of horizontally sheared flow seen in the observations are generally not accurately captured by the models, with SODA and ORAS4 showing rather large-scale patterns only (typically spanning most of the C-PB transect). Only ORCA12 exhibits sharp current reversals along the section, in the season of northward-flowing EICC (February-July) as well as in the opposite situation (November).

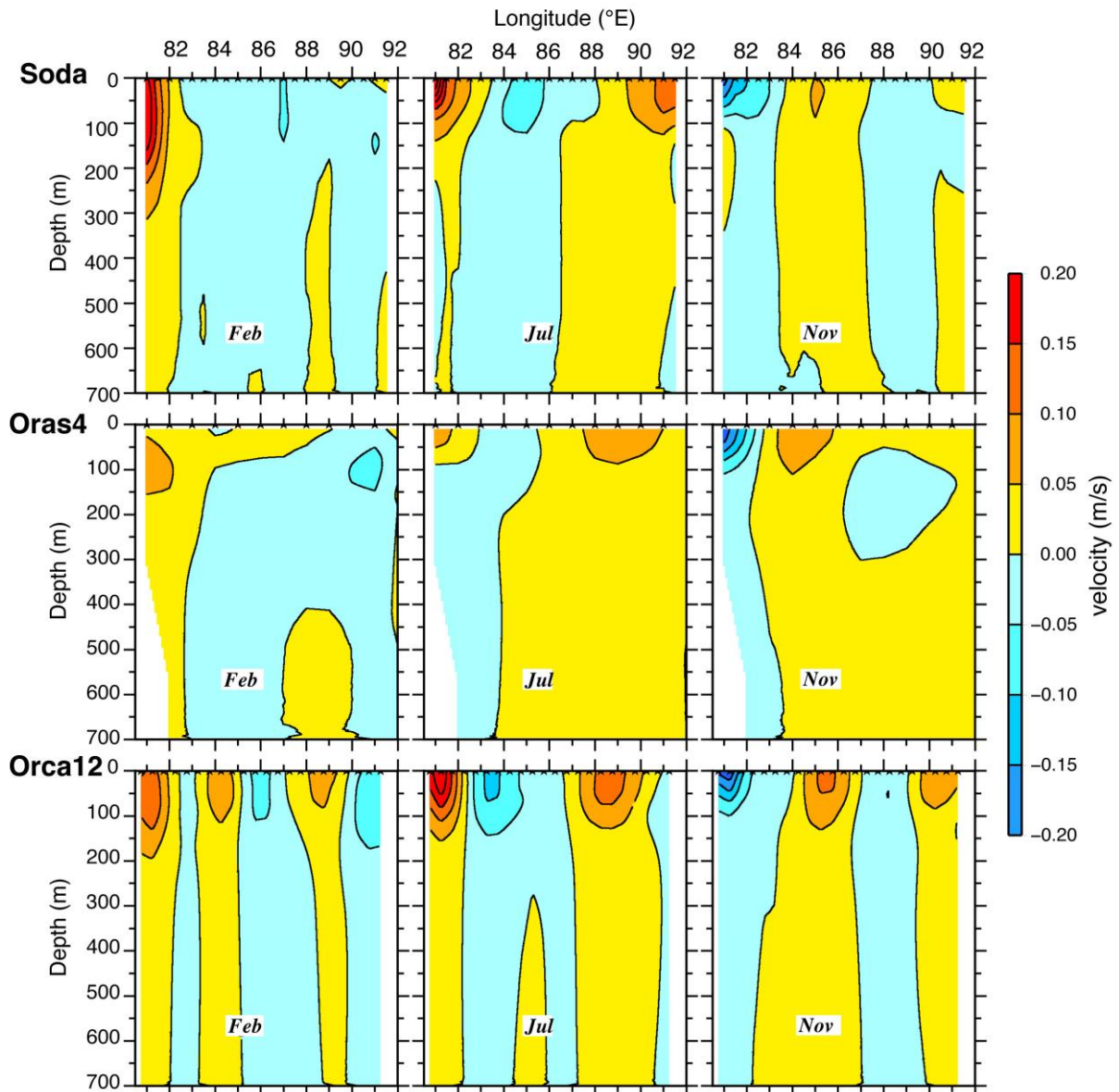


Figure 3. Monthly climatology of the modelled geostrophic current projected in the cross-track direction along C-PB route, for February (1st column), July (2nd column) and November (third column). SODA is on first row, ORAS4 on second row and ORCA12 on third row. Positive values indicate northward flow. The contour interval is 0.05 m/s.

Figure 4 presents the standard deviation of our monthly climatology along the C-PB transect. It was computed after removing the long-term mean of the monthly climatology. As expected from the seasonal cycle that was described for Figure 2, a core of maximum variability is observed in the boundary region between 81°E and 82°E, over the upper 200m. The maximum value is $0.13\text{m}\cdot\text{s}^{-1}$ at 81.25°E and 40 m depth. This region is located at the offshore edge of the continental slope area. Based on this structure of the mean flow and its seasonal variability, we define a section from 80.75°E to 82.25°E and use this section to compute the volume transport of the EICC. Figure 5 presents the seasonal evolution of this

volume transport for our dataset as well as for the three numerical products. The observed transport is poleward throughout the January–September period but has varying intensity, reaching peak values of 5 Sv in February, April and July. Then, the flow reverses to a peak value of 4 Sv equatorward in November. Consistent with the past studies, we confirm that the possible window of fresh water export out of the BoB through its western boundary current is limited to the October–November period.

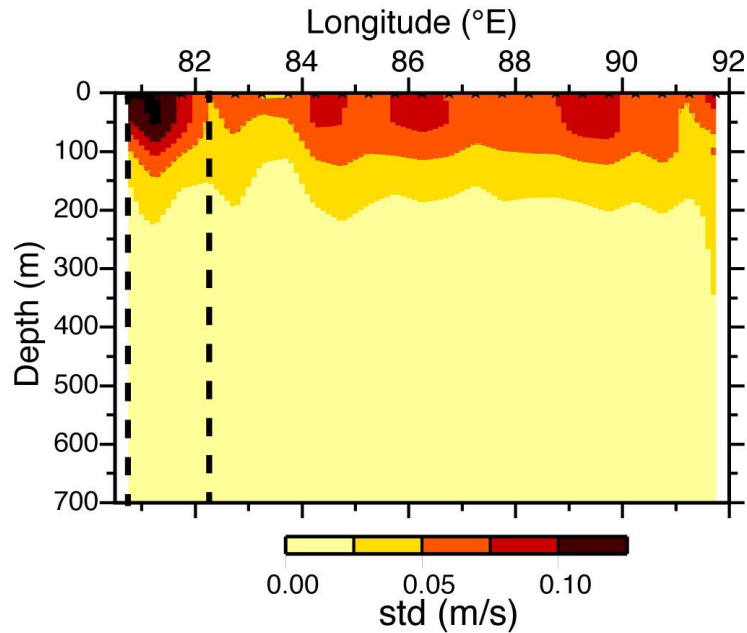


Figure 4. Standard deviation of the seasonal climatology of observed cross-track geostrophic current along the C-PB route. The contour interval is 0.025 m/s. The dashes (80.75°E – 82.25°E) define the domain of the EICC.

For all three models, volume transport estimates follow a seasonal evolution similar to our observations. SODA and ORCA12, however, over estimate the March–May flow (by a factor of 1.8 for SODA and 2.5 for ORCA12). The magnitude of interannual variability of SODA and ORCA12 is in line with our observations. The transport derived from ORAS4 reanalysis stands at odds with the observed evolution. The main drawbacks are its early reversal of the transport simulated in July and its extremely weak magnitude of interannual variability around this seasonal cycle, seen in all seasons.

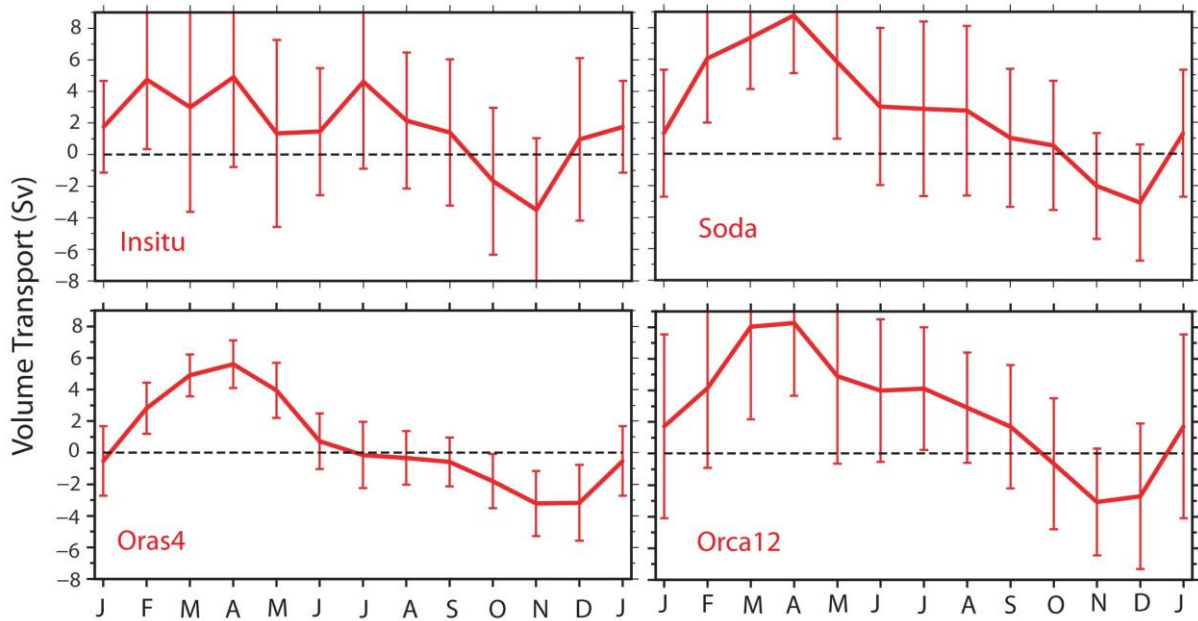


Figure 5. Observed and modelled seasonal climatology of EICC transport (domain defined on Figure 4) along the C-PB route for *in situ* observations and for the various model solutions. The vertical bars (+/- one standard deviation) show the magnitude of the interannual variability around the climatology.

3.2 Interannual variability

The 27-year duration of our observational record provides the opportunity to investigate year-to-year deviations around the seasonal evolution that was previously described. We computed monthly interannual anomalies of the current with respect to our monthly climatology along the C-PB route. From these interannual anomalies, we computed their standard deviation directly (since they have, by definition, a null mean). Figure 6 shows the standard deviation of these current anomalies for our observations as well as for the three numerical products. Similar to the seasonal variability we already discussed, the observations exhibit a variability prominently located in the boundary region, to the west of 82°E. The maximum value is $0.26 \text{ m}\cdot\text{s}^{-1}$ at 81.25°E at the sea surface, which is approximately twice as large as the seasonal standard deviation there. Such a large magnitude of interannual standard deviation, two times stronger than the seasonal standard deviation, is observed over most of the C-PB transect, in the upper layer as well as at subsurface. Hence, we confirm the dominance of the interannual variability over the seasonal variability of the western boundary current, as was reported by Durand et al. (2009) for the surface layer. In addition, we show that this interannual dominance does not concern only the surface but also extends to the thermocline and subthermocline layers. Mukherjee et al. (2014) also reported the dominance of non-seasonal variability of along-shore current on the shoreward edge of the slope in the

western BoB. Our observations prove that this is also true throughout the basin, from the continental slope to the Andaman Islands.

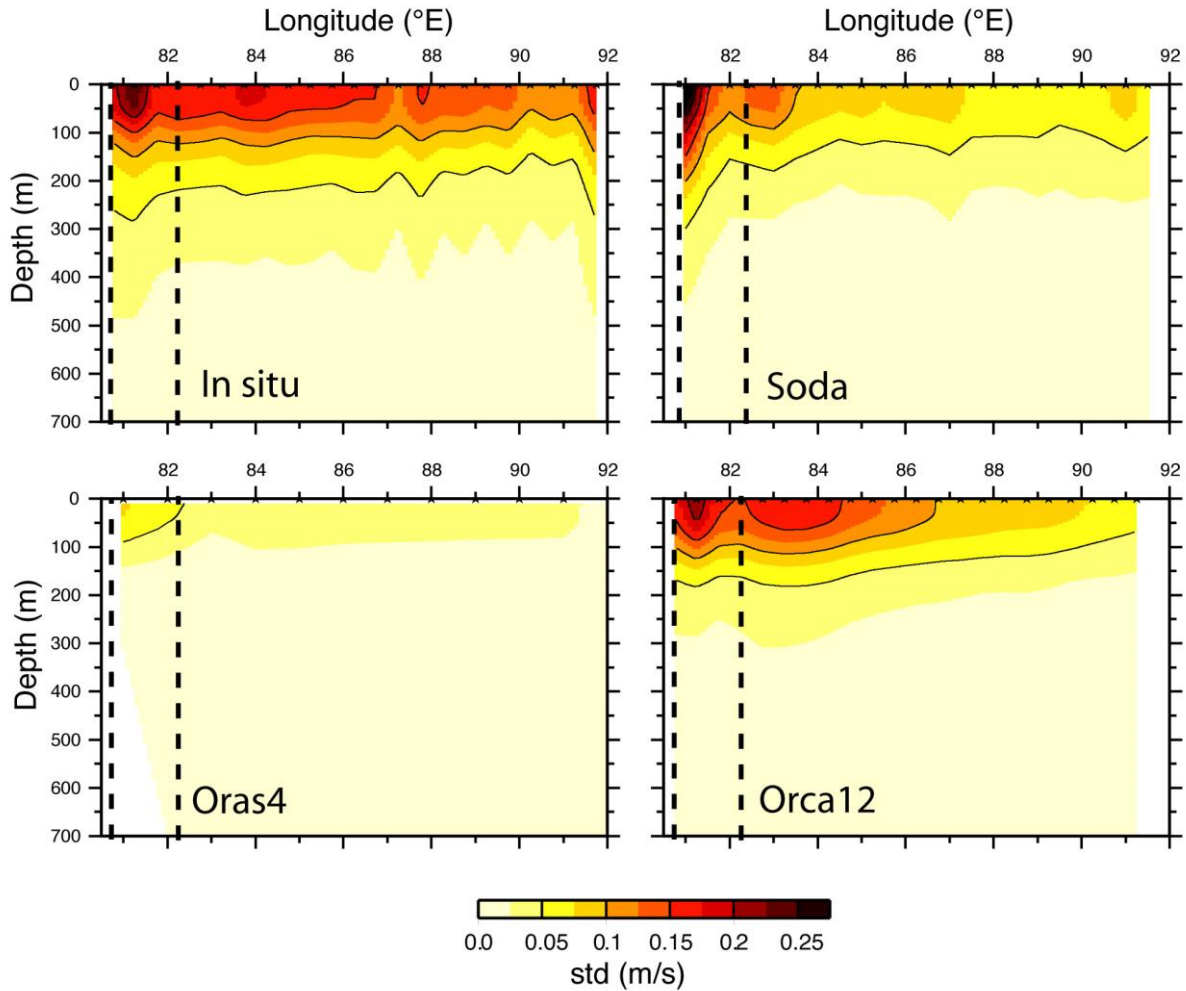


Figure 6. Standard deviation of the interannual anomalies of cross-track geostrophic current along the C-PB route for *in situ* observations (top, left). Standard deviation of interannual anomalies of model geostrophic current projected in the cross-track direction along the C-PB route for SODA (top, right), for ORAS4 (bottom, left) and for ORCA12 (bottom, right). The contour interval is 0.025 m/s. The dashes (80.75°E – 82.25°E) define the domain of the EICC.

Figure 6 also shows the section of interannual variability reproduced by the three numerical products. All three models successfully capture the observed coastally trapped core of maximum variability, decaying eastward. However, the magnitude of the variability appears to be highly model-dependent, with a clear overestimation in SODA at the shoreward edge of the domain and an underestimation in its eastern part. ORAS4 consistently shows an underestimation of the variability at all longitudes. ORCA12 appears to be the most realistic of the three products, though with a slight underestimation of the variability offshore the EICC domain.

4. Relationship between EICC variability and IOD activity

The prominence of interannual variability of the EICC over its seasonal cycle motivates this section. As mentioned in introduction, only a handful of studies have investigated the origin of interannual variability of the EICC and are based mostly on numerical models due to the lack of pluri-annual observational records (Rao et al., 2002; Thompson et al., 2006; Jensen, 2007; Aparna et al., 2012). As they all have pointed towards the wind anomalies during IOD events in the generation of anomalous upper BoB circulation, this section is dedicated to the analysis of the IOD-related anomalies in our observational record.

4.1 Composites of current

To highlight the signatures of IOD events in our observational dataset, we composited the monthly current anomalies for positive IOD events (PIOD), negative IOD events (NIOD) and neutral years. The IOD years were defined based on the Dipole Mode Index (DMI), available on stateoftheocean.osmc.noaa.gov/sur/ind/dmi.php. The corresponding years are listed in Table 1. As the IOD events usually reach their peak in the fall season, Figure 7 presents the September-October-November composites for our current dataset. The PIOD composite shows a northward anomaly at the western boundary in September (to the west of 82°E), with a maximum value of 0.2 m.s⁻¹ at the surface, extending downward to approximately 300m. In October, this poleward anomaly extends offshore to 83°E and remains unchanged in November. The October–November anomalous pattern in the EICC domain is commensurate with and even slightly superior to the climatological EICC velocity observed there (as seen in Fig. 2) but with an opposite sign. It thus amounts to a reversal of the flow compared to climatological conditions. Eastward of the EICC domain, alternating bands of northward and southward anomalies are observed, generally surface-intensified and typically extending downward to 300m.

PIOD years	1991, 1994, 1997, 2006, 2008, 2011, 2012, 2015
NIOD years	1992, 1996, 1998, 2010, 2016
neutral years	1993, 1995, 1999, 2000, 2001, 2002, 2003, 2004, 2005, 2009, 2013, 2014

Table 1. List of positive IOD events, negative IOD events and neutral years in our observational period.

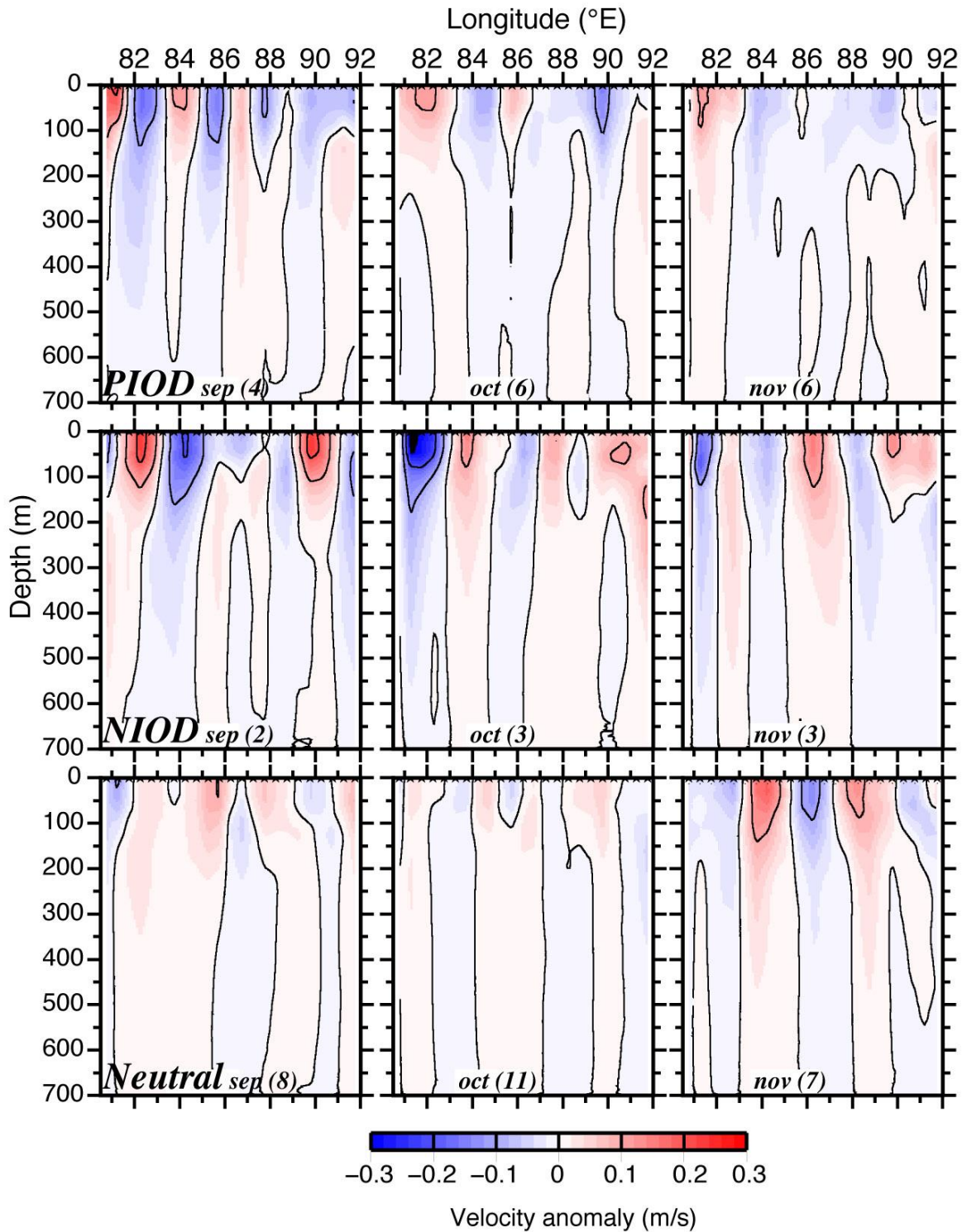


Figure 7. Observed composites of interannual anomalies of the cross-track geostrophic current along the C–PB route during (top) positive IOD years, (middle) negative IOD years, and (bottom) neutral conditions; the left column is for September, the middle column is for October, and the right column is for November. The contour interval is 0.1 m/s. Positive values indicate northward current anomalies. The number of individual cruises used to compute each monthly composite is indicated between brackets.

The situation in the NIOD composite basically shows an opposite pattern, with a southward anomaly appearing at the western boundary (81°E) in September, picking up and extending downward and offshore (to 83°E) by October, and decaying in November. At its peak in October, surface velocity anomalies in excess of 0.3 m.s⁻¹ are observed near 81.75°E, hence amounting to a three-fold increase in the climatological southward flow there. Offshore, just like for the PIOD composite, alternating bands of northward and southward flow anomalies are seen, surface-intensified and extending throughout the upper 700m. As for the neutral years composite (in the sense: neither positive IOD nor negative IOD), moderate and insignificant anomaly patterns are seen in the EICC domain, with still a striation of northward and southward veins throughout the section, extending from the surface to 200–300m in all months.

4.2 Composites of transport

As the anomalous patterns of the EICC captured by our composites appear strong, broad, and extend over a thick layer, we computed the corresponding transport anomalies of the EICC. Figure 8 presents the August–January evolution of these transport anomalies for the PIOD and NIOD composites, for our dataset as well as for the three numerical products.

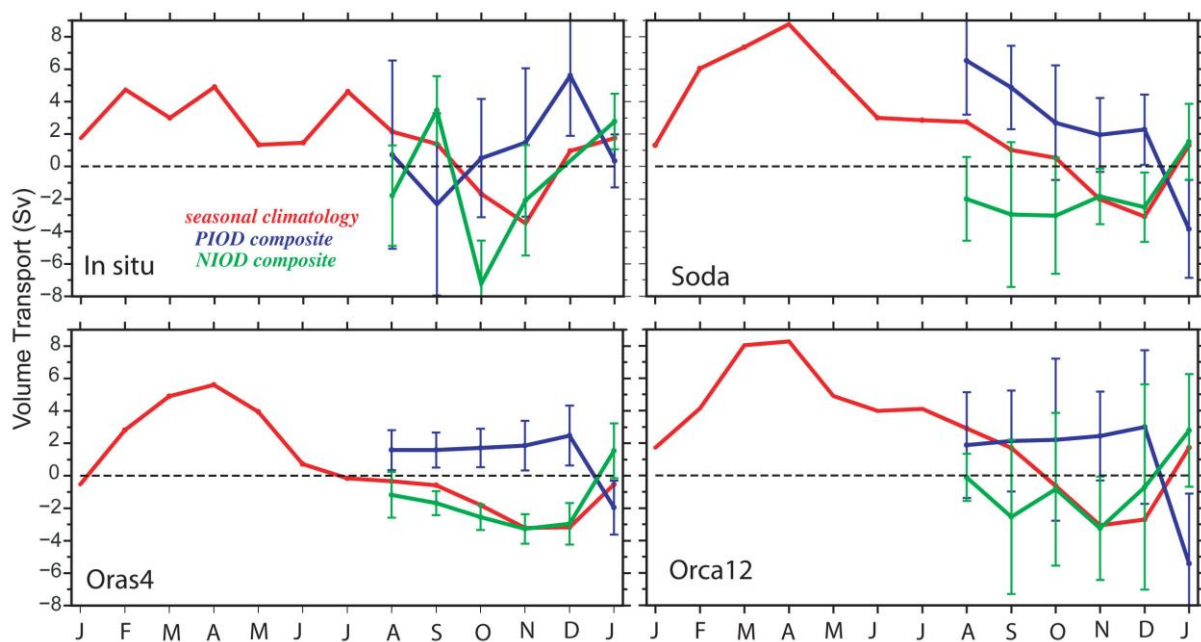


Figure 8. Same as Figure 5, with fall-winter evolution of the transport anomalies for positive IOD composites (blue) and negative IOD composites (green) superimposed (the domain of integration is shown on Figure 4). The vertical bars(+/- one standard deviation) show the magnitude of the variability around the composites.

During a PIOD event, a northward anomalous EICC transport appears in October, picks up in November and reaches its peak in December at 5.5 Sv. Then, it vanishes. Conversely, during a NIOD event, the EICC turns suddenly from anomalously northward (3.5Sv) in September to anomalously southward (-7Sv) in October, then decays through November–December.

Although the pattern of interannual variability simulated by SODA was quite realistic (Fig. 6), this product appears unable to capture the seasonal timing of the development of this northward (during PIOD years) and southward (during NIOD years) EICC transport anomalies: in both cases, SODA exhibits strong anomalies (though of the right sign) as early as August–September, completely collapsing afterwards. The NIOD anomalies simulated by ORCA12 have the correct sign as well (negative until December), but they also fail to reproduce the magnitude shown in the observations. The PIOD anomalies simulated by SODA show an unrealistic decrease from 6 Sv in August to 2 Sv in December, which is inconsistent with the large increase observed over this period. ORCA12 shows a moderate increase of the PIOD anomaly during the same period, from 2Sv in August to 3Sv in December. As for ORAS4, consistent with its known serious underestimation of the magnitude of interannual variability, the evolution of both PIOD and NIOD transport composites is quite sluggish, hardly exceeding 2Sv in absolute values in November–December. Their sign, however, is in line with the observed dataset, with a peak northward anomaly in December for PIOD events and a southward anomaly in October–December for NIOD events.

In addition to the seasonal evolution of the anomalous EICC transport during PIOD and NIOD years, Figure 8 also shows the standard deviation of the anomalous transport (seen in the vertical bars) for each composite. This shows that their event-to-event deviation is large in our dataset, typically of same order as the composite magnitude itself, for most of the months: this implies that even the direction of the transport anomaly (southward vs. northward) is not totally robust during a particular IOD event. Only at the time of peak values (northward peak in December for PIOD years, southward peak in October for NIOD years) does the sign of transport anomaly appear roughly robust from event to event.

In both the SODA and ORCA12 models, this event-to-event variability is as strong as in the observations, making the direction (northward/southward) of their simulated anomalous transports also not robust. Only ORAS4, because of its excessively low variability, reproduces consistent transport anomalies during PIOD as well as during NIOD events.

In brief, the observations reveal a distinct evolution of post-monsoon EICC transport during IOD events, with a northward anomaly during PIOD years and a southward anomaly

during NIOD years. The magnitude of these anomalies is superior to the magnitude of the seasonal climatology of the EICC transport (southward in this season). Hence, a complete reversal of the EICC transport can be expected during PIOD events (with a northward transport), and a two- to three fold increase of the southward EICC transport during NIOD events, compared to climatological conditions. However, the event-to-event differences appear strong, hereby suggesting that one cannot easily predict the magnitude of the anomalous transport during a particular IOD event. All three models present different skills to reproduce the canonical IOD transport, with ORCA12 and SODA relatively more capable of capturing the magnitude, spread (and, to a lesser extent, the timing) of the anomalous EICC transport as the events develop from September through December; ORAS4 underestimates both the magnitude of the composites as well as the magnitude of their spread.

4.3 An "IOD mode" revealed by EOFs

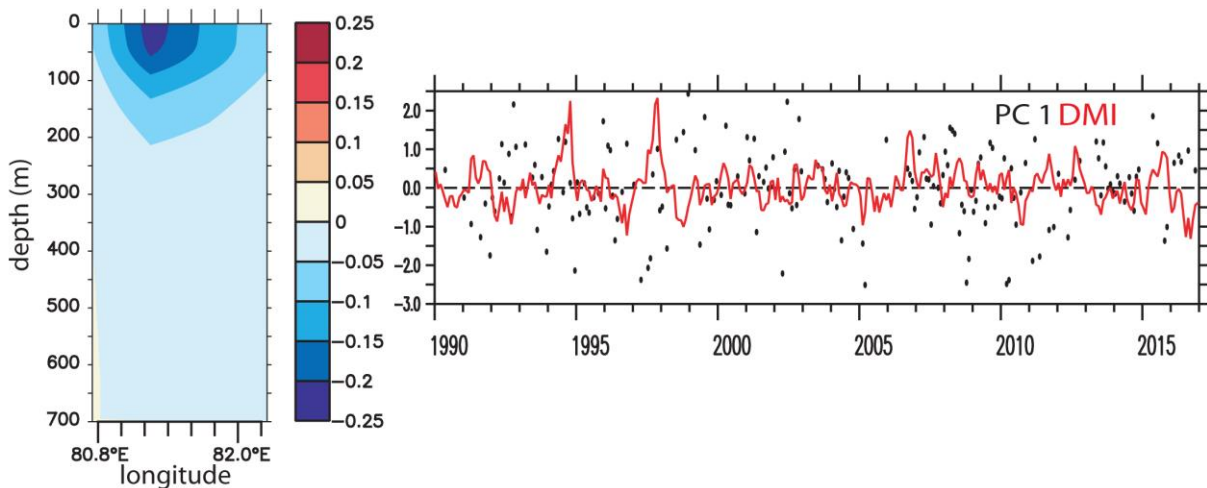


Figure 9. First EOF mode (left) and first principal component (right, black dots) of observed EICC interannual anomalies along C–PB route, from 1990 to 2016. Time evolution of DMI index is superimposed (right, red).

As noted above, the IOD-related variability of the EICC is evident in our observations, both in terms of velocity and of integrated transport. However, the event-to-event differences are strong for PIOD as well as NIOD events. To further characterise the part of the variability of the EICC that is linked with IOD activity compared to the part that could be forced by other phenomena, we operated an empirical orthogonal function (EOF) decomposition of our observed monthly interannual current anomalies (considered over the EICC domain only: 80.75°E–82.25°E). The first EOF mode is displayed in Figure 9. This dominant mode

accounts for 44% of the total variance of interannual EICC. The other EOF modes account for a minor part of the total variance (25% for the second mode, 16% for the third mode, etc.), which are not discussed here. The spatial structure of the first mode is reminiscent of the canonical pattern of IOD composites discussed in the previous section, with a surface-intensified core spanning the entire longitudinal range of the EICC (from 80.75°E to 82.25°E), extending downward to approximately 200m. Figure 9 also presents the principal component time-series of the first mode (from 1990 to 2016), along with the DMI evolution. It is apparent that the two time-series tend to vary in phase opposition, with positive peaks often associated with NIOD events, and negative peaks often associated with PIOD years. Given the negative sign of the spatial pattern of the mode, this is consistent with the PIOD and NIOD current composites discussed in previous paragraphs. For convenience, we term this first EOF mode as "IOD mode" in the following. The lagged correlation between DMI and the first mode principal component (September-October-November period only) amounts to -0.45 with two months lag (with EOF principal component lagging behind DMI; significant at 99% confidence interval) and decreases to -0.08/-0.32 at null lag/1 month lag, respectively.

We operated a similar EOF decomposition of the current simulated by SODA, ORAS4 and ORCA12 models. All three products revealed a dominant IOD-like mode similar to Figure 9 (not shown). The correlation of their principal component time-series with DMI time-series, however, significantly differed from model to model, with values at 2 months lag amounting to -0.47 (SODA) / -0.56 (ORCA12) / -0.83 (ORAS4), all significant at more than 99%. Clearly, ORAS4 overestimates the statistical relationship between EICC interannual variability and IOD activity. SODA and ORCA12 are more in line with the observed correlation value.

5. Kolkata–Port Blair transect

Although the observational coverage of our *in situ* dataset along the K–PB transect is significantly less dense than along the C–PB sector (Fig. 1), it is still relevant to investigate the seasonal evolution of the cross-track circulation there and to document, at least partly, its interannual variability. The K–PB transect intersects the slope region at 19°N, off the Hooghly river mouth (Fig. 1). The K–PB transect is situated approximately 1200 km upstream of the C–PB, along the coastal waveguide of the BoB. Our monthly climatology of geostrophic current across the K–PB transect is represented in Figure 10. A prominently eastward flow is observed between 18°N and 20°N (corresponding to the slope region), spanning the entire range of depths from surface to 700 m, with varying intensity from season to season: it is stronger in winter (December–March) and vanishes during summer (July).

South of 18°N, the cross-track current is generally weaker than in the slope region, and of variable direction. This prominent eastward flow in the northward part of our transect dominates the long-term mean current shown in Figure 11, with a core of maximum current (over 0.05 m.s⁻¹) situated above 100 m, from 18°N to 20°N. North of 19.25°N, the mean flow remains eastward down to 700 m. This region of the thickest EICC corresponds to its region of maximum variability (Fig. 11), with standard deviation of the flow being much larger than its long-term mean at all depths. These characteristics of the EICC appear to be consistent with the ADCP mooring record of Mukherjee et al. (2014) that was deployed at 19°N, within 40 km of our nominal ship track.

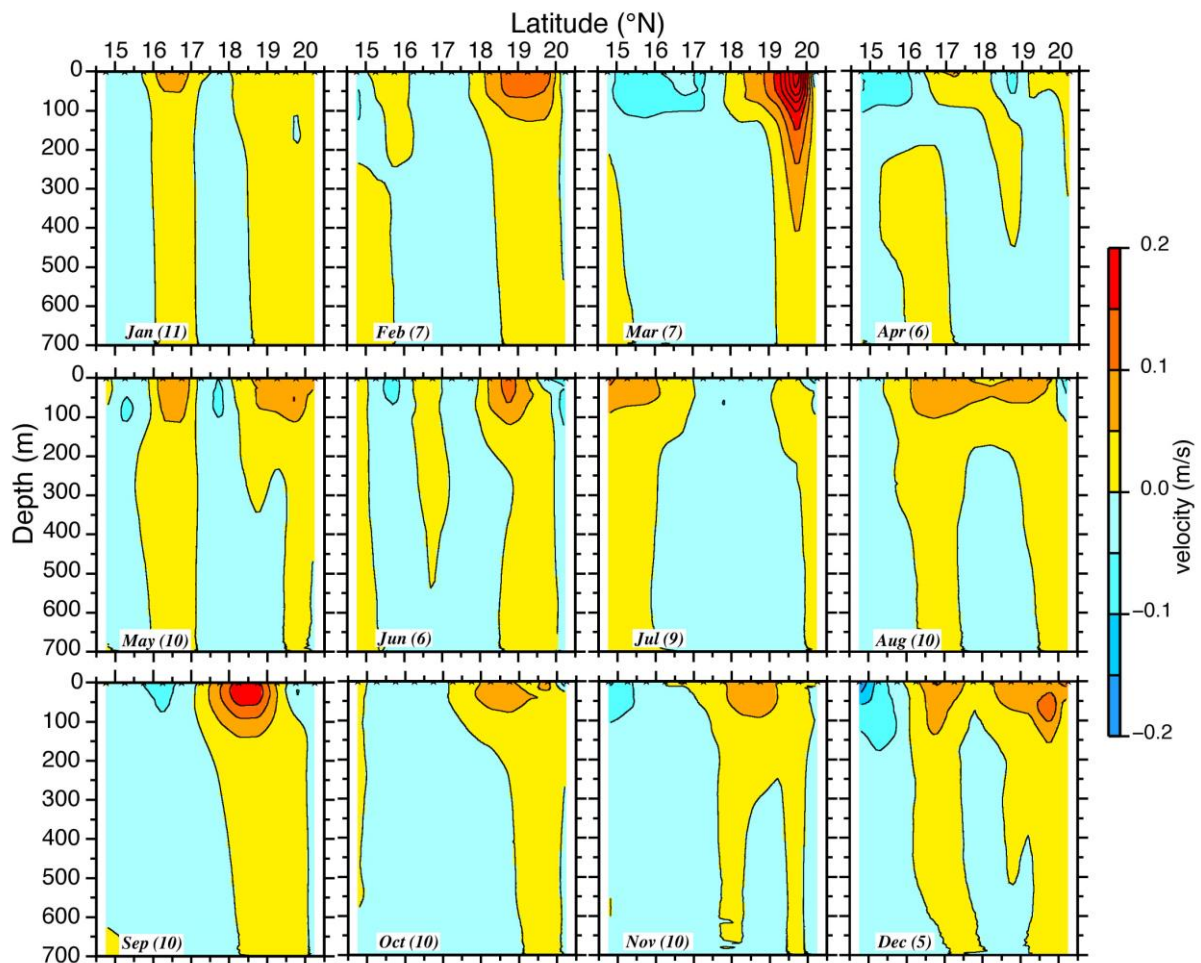


Figure 10. Monthly climatology of observed cross-track geostrophic current along the K–PB route. The number of individual cruises used to compute each month climatology is indicated between brackets. Positive values indicate north-eastward flow. The isocontour interval is 0.05 m/s.

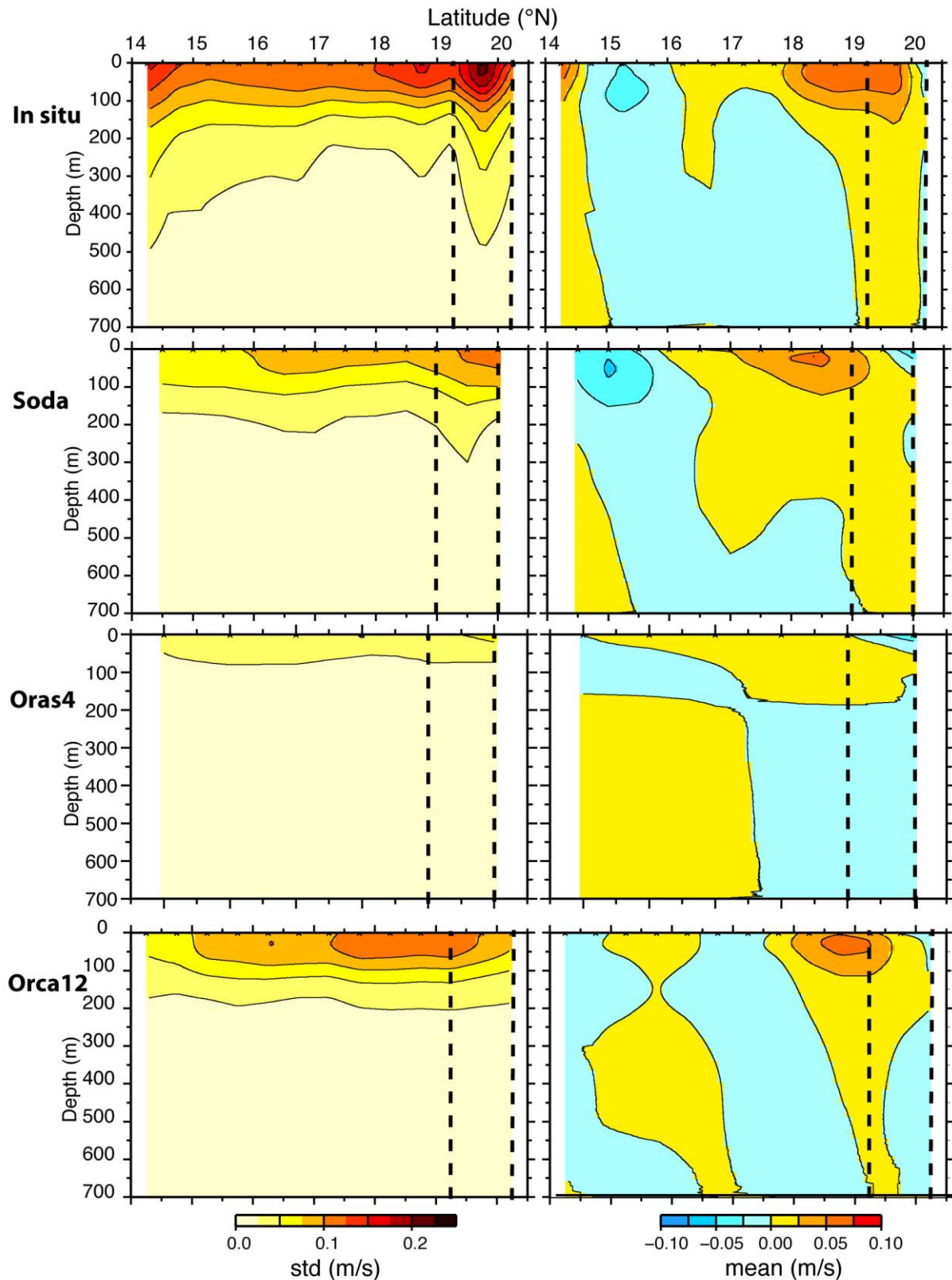


Figure 11. (first row) Standard deviation (left) and mean (right) of the observed cross-track geostrophic current along the K–PB route. The contour interval is 0.025 m/s. The dashes (19.25°N - 20.25°N) define the domain of the EICC. The second, third and fourth row show the same for SODA, ORAS4 and ORCA12, respectively.

We also present in Figure 11 the long-term mean and variability of the three numerical products. All three models agree in simulating a mean eastward flow in the upper (above 200 m typically) and northern (north of 16°N) part of the K–PB transect, comparable with the observations. Regarding the variability, all three models concur in simulating a surface-intensified pattern, extending to a greater depth in the northern part of the transect (to the north of 19°N). However, ORCA12 appears to capture the pattern of current variability better than the other two models, with a surface-intensified structure exceeding 10 cm/s between 17.5°N and 19.5°N, but with values lower than the observed ones. SODA also shows a reasonable ability to capture the pattern and intensity of flow variability, but with even lower magnitude. SODA, however, captures to some extent the observed deepening of the core of maximum variability centered on 19.5°N. ORAS4, in contrast, completely underestimates the current variability at all depths throughout the K-PB transect. Regarding the mean flow, ORAS4 shows a very weak current vein (which nowhere exceeds 2.5 cm/s), located too far south (by approximately 100 km, around 17°N-19°N). ORCA12, in particular, mimics the observed pattern reasonably well, with a narrow, thin and intense core of mean eastward flow, alike the observed pattern (but still hardly extending north of 19.5°N).

This distinct skill of the three numerical products evidenced by Figure 11 further reflects in their different abilities to simulate the patterns and timing of the seasonal evolution of the current (Fig. 12). Based on the evolution of observed seasonal flow, we present the periods of peak eastward flow (March), minimum flow (July) and moderate eastward flow (November) of the boundary current. All three models represent the observed patterns rather poorly. In March, all of them simulate an eastward boundary current, but hardly crossing $0.1\text{m}\cdot\text{s}^{-1}$ and extending no deeper than 200 m. In July, all models simulate a realistic weak flow but with an erroneous eastward direction at depth throughout the south-central part of the section, whereas the observed current is westward there. The moderate eastward-flowing current observed in November between 18°N and 19°N is adequately captured by SODA and ORCA12 (both in magnitude and in vertical extent) but is completely missed by ORAS4.

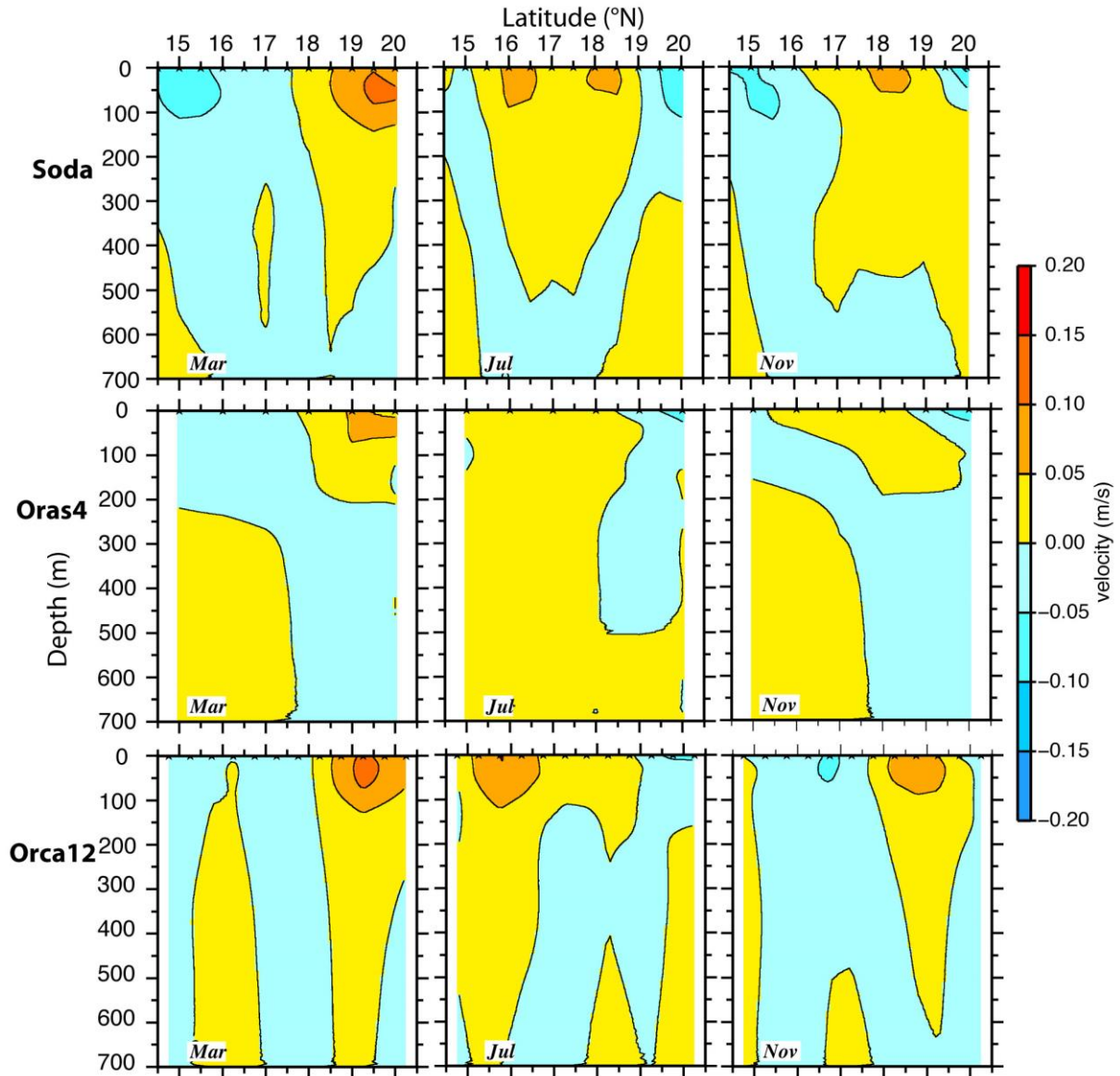


Figure 12. Monthly climatology of the modelled current projected in the cross-track direction along K–PB route for March (1st column), July (2nd column) and November (third column). SODA is on the first row, ORAS4 on the second row and ORCA12 on the third row. Positive values indicate north-eastward flow. The contour interval is 0.05 m/s.

Based on the observed coastal trapping of the standard deviation of the current (Fig. 11), we defined the 19.25°N–20.25°N latitudinal band for what we hereafter term as EICC, along the K–PB transect. Similar to what we did along the C–PB transect, we computed the volume transport of the flow through this area. Figure 13 shows the observed seasonal evolution of this EICC transport. Consistent with what was seen in Fig. 10, the February–March period stands out as the sole period of significant transport of the EICC. The peak eastward transport is 7 Sv in March. This strong transport immediately collapses in April and remains close to zero throughout the rest of the year. The standard deviation of the transport

around this monthly climatology is strong compared to the magnitude of the seasonal climatology, in all months. Similar to the EICC transport along the C-PB, the magnitude as well as the direction of the seasonal flow are not robust along the K-PB from year to year. One exception is the March eastward peak, of which the magnitude (7Sv) is slightly superior to its interannual standard deviation (plus or minus 6 Sv). Figure 13 also shows the corresponding seasonal climatology of the EICC transport for the three numerical products. Both SODA and ORCA12 bear some similarities with the observed evolution, although they basically miss the peak eastward transport in March and simulate an erroneous westward transport in June-August. The magnitude of their interannual standard deviation is in line with the observed dataset, hereby confirming the non-robust direction of the EICC climatological transport in all seasons. ORAS4 simulates a very weak EICC transport in all seasons and misses the March eastward peak, similar to the other two products. In contrast with the other two products, ORAS4 completely underestimates the magnitude of year-to-year standard deviation in all seasons.

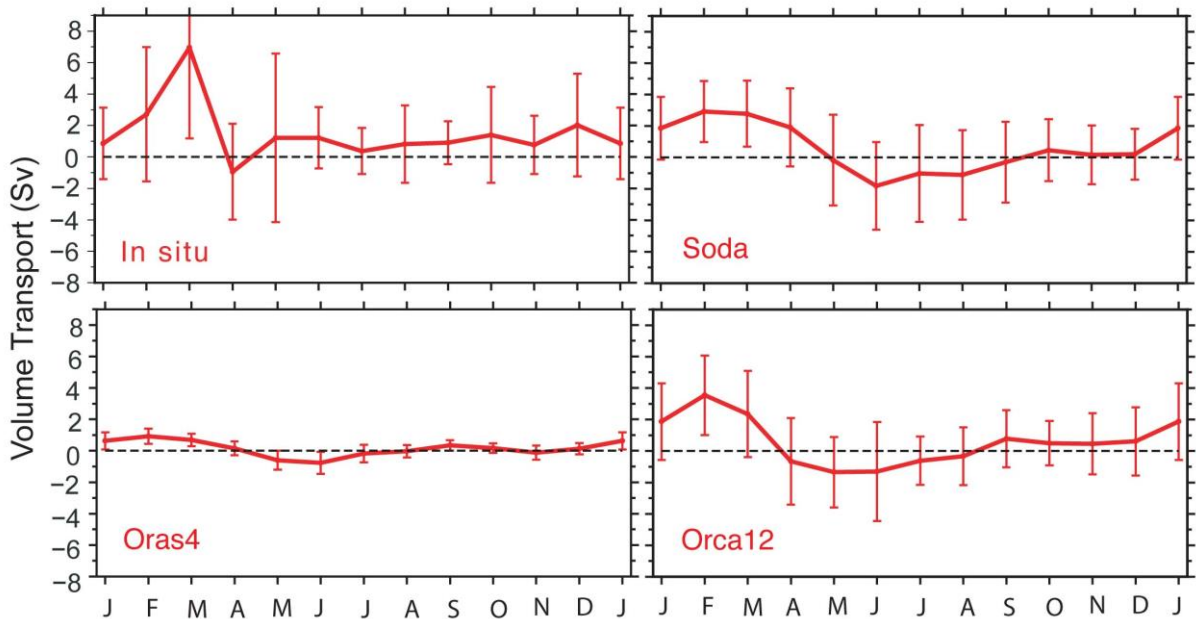


Figure 13. Same as Figure 5, but for the K–PB route. The domain of integration of the EICC transport ($19.25^{\circ}\text{N} - 20.25^{\circ}\text{N}$) is shown in Figure 11.

6. Discussion and conclusion

The dataset used in this study is a 27-year-long record of repeated XBT transects. We described the western boundary current of BoB, known as the EICC. We focused on its horizontal and vertical characteristics and on its transport, successively in terms of seasonal climatology, long-term mean and inter-annual variability. Earlier descriptions of the EICC

current and transport were based on one-time cruises conducted in various seasons (e.g.; Shetye et al., 1991, 1993, 1996; Sanilkumar et al., 1997), numerical models (e.g., McCreary et al., 1996; Shankar et al., 1996; Vinayachandran et al., 1996; Rao et al., 2002; Aparna et al., 2012; Suresh et al., 2013), space-borne altimetry (Durand et al., 2009) or point-wise current-meter records (Mukherjee et al., 2014). Our study thus appears very complementary to the past papers, thanks to its unprecedented space-time observational layout. The long-term mean and seasonal evolution of the EICC revealed by our dataset is in agreement with earlier studies. In the western BoB (C-PB transect), we confirmed poleward flow during the spring and summer with a peak during February–April, and an equatorward flow during November. In the north-western BoB (K-PB transect), we observed a prominent eastward flow throughout the year that intensified in March. IOD events have a clear impact on EICC transport variability, with poleward anomalies during PIOD years and equatorward anomalies during NIOD years in the post-monsoon season.

6.1 Salient novel findings

Our dataset revealed the dominance of non-seasonal anomalies of the flow over the seasonal climatology. The magnitude of the standard deviation around the seasonal evolution indeed points to a marked year-to-year modulation, in such a way that the seasonal picture can be completely distorted in a given year. This prominent non-seasonal flow exists in the western BoB (C-PB) as well as in the northern BoB (K-PB). This finding concerns the surface as well as the thermocline and subthermocline layers.

We concluded that the core of the EICC mean seasonal transport, as well as its core of maximum variability (both seasonal and interannual), are situated at the offshore edge of the slope region. The integrated, long-term *in situ* observational records of the EICC variability analysed by Mukherjee et al. (2014) in the slope region shed light on interesting and novel characteristics of the western boundary regime. However, the structure of the flow in the cross-shore direction revealed by our dataset merits a re-visit of Mukherjee et al.'s (2014) investigations, with an observational network displaced further offshore than theirs. This is timely because the EICC is a main component of the climatic system in the BoB.

We confirmed that the post-monsoon season (October–November–December) is the sole period when a southward export of upper BoB waters through the WBC exists in the seasonal climatology. However, the interannual deviation of the post-monsoon flow velocity is high enough that, in many years, the post-monsoon export of BoB water through the western boundary may simply not occur. The canonical view shown by our IOD composites reveals an enhanced (threefold) southward transport of the EICC during NIOD years in the post-

monsoon season. Conversely, in our PIOD composite, the post-monsoon window of southward BoB water remains closed. The two-month lag between IOD activity captured by DMI and the response of the EICC velocity off Chennai is consistent with the previously proposed mechanism of remote forcing involving baroclinic Kelvin waves generated by anomalous wind patterns in the equatorial Indian Ocean and travelling through the rim of the Bay of Bengal (Rao et al., 2002; Aparna et al., 2012). With regard to our observational approach, which is based on repeated XBT surveys, it must be stated that our transport estimates do not account for any ageostrophic component of the flow such as the Ekman current. Considering the multi-year GEKCO current product of Sudre et al. (2013), we could conclude that the Ekman transport integrated over the EICC domain (as defined previously) is typically inferior to 0.3 Sv in absolute value for both the C–PB and K–PB routes, with long-term means inferior to 0.1 Sv. This implies that our geostrophic transport estimates can be considered as accurate within 0.3 Sv. Beyond this, the lateral physics of the western boundary currents are known to be influenced by viscous processes. Similarly, the momentum dissipation in the bottom boundary layer is also prone to significantly distort the geostrophic flow. The need for quantitatively assessing the role of these processes further calls for a revisit of the Mukherjee et al. (2014) observational strategy, based on *in situ* measurements of the absolute flow velocity. Another limitation of our observational dataset lies in the horizontal resolution of our casts along the transects. They typically do not allow to resolve the imprint of mesoscale eddies, given the observed size of these features (see, e.g., Durand et al. 2009). The numerical study of Cheng et al. (2013) concluded that the EICC is significantly unstable at intra-seasonal timescales and yields mesoscale eddies through baroclinic instability. Documenting this process through an enhanced *in situ* observational network appears to be highly relevant.

6.2 Assessment of numerical models

The three state-of-the-art numerical products we considered (SODA, ORAS4 and ORCA12) revealed a highly variable degree of realism in the EICC velocity and transport, for the mean, seasonal variability as well as interannual variability of EICC. Among the numerous limitations identified, most are model-dependent. Pinpointing the reasons for model deficiencies is clearly beyond the scope of the present study. However, it clearly appears that the coarse resolution of ORAS4 (and, to a lesser extent, of SODA) does not help in a western boundary eddy regime such as the EICC. In line with the observations of Durand et al. (2009), a strong horizontal shear is seen in the observed flow at all timescales, extending throughout the two transects from the India mainland to the Andaman Islands. Among the

various models we considered, only the eddy-resolving ORCA12 manages to simulate this sheared structure in the flow velocity outside the boundary domain. This model reproduces significantly more variability than the other two all along the transects. This points towards the likely limitation of the coarser grids of ORAS4 and SODA. This conclusion is in line with Benschila et al. (2014), who compared eddying ($1/12^\circ$) and coarser ($1/4^\circ$) versions of the NEMO model over the BoB. In the course of 2018, new global reanalysis products at $1/12^\circ$ resolution are expected to become available as part of the CMEMS framework (Copernicus Marine Environment Monitoring Service, see marine.copernicus.eu). Comparing such products with the existing coarser reanalyses would likely help to understand the effect of model grid resolutions. The sidewall boundary condition for momentum was also illustrated by Benschila et al. (2014) to be a key ingredient of the realism of EICC velocity in the upper 300 m, particularly in the peak flow seasons (inter-monsoons). For ORAS4, despite the sophisticated data assimilation scheme operated in this system, the resulting reanalysis considerably lacks variability in the simulated EICC. SODA and ORCA12, despite their ability to appropriately capture the magnitude of the interannual variability of the EICC, fail in reproducing the details of the IOD-related patterns of anomalies. This is surprising, since the known mechanism that explains the link between IOD activity and EICC variability essentially involves linear dynamics through long baroclinic waves usually properly simulated by this class of general circulation models. This may point towards the inadequate impact of the data assimilation procedure in the SODA system. The reason for this remains unclear to us.

One drawback common to all models is their general inability to accurately capture the exact pathway of the EICC in the slope region of the northwestern BoB (K-PB transect): whereas the observations show that it flows prominently at the offshore edge of the slope region, the various models place it too far offshore. One possible solution may be to further increase the horizontal resolution of BoB circulation models to a stage where the coastal frictional layer is explicitly resolved (typically, at kilometre scale). To the best of our knowledge, such models do not yet exist over our area. This echoes to the past studies of Chao et al. (1996) or Sérazin et al. (2015), who attribute their better modelling of current mean paths to the better resolution of the models they used. Our *in situ* dataset, primarily falling within the Indian Economic Exclusive Zone (EEZ), it is not routinely incorporated in the international data portals, and hence it is not assimilated by the ORAS4 and SODA pipelines. In this sense, our inter comparison can be considered to be an independent validation of these reanalysis products. Given the discrepancies observed between our data

and the reanalyses, our study calls for a dedicated data assimilation exercise of our dataset, aiming towards the future generation of reanalysis products over the BoB.

6.3 Interannual variability not related to IOD

We observed that there is a distinct signature of IOD activity in the current and transport anomaly composites. However, the IOD mode identified by our EOF decomposition accounts only for approximately 44% of the total interannual variability of the EICC. Other processes of the EICC variability must be considered. The western boundary current of the BoB is a region of intense eddy activity (Chen et al., 2012; Cheng et al., 2013). Mesoscale meanders and eddies are generated along the EICC path by instability of the background flow. Open-ocean eddies can also impact the EICC flow because of their tendency to migrate westward after their generation in the central and eastern BoB. According to Sérazin et al. (2015), although the large scale, low-frequency variability is mainly driven by the atmosphere, in eddy-active regions (such as the western BoB), intrinsic turbulent processes typically contribute 30% to 50% of the variance of sea level (a variable tightly connected to upper ocean circulation). Hence, non-linear turbulence may have an influence commensurate with linear, wind-driven forcing in the non-seasonal modulation of the EICC we observe. The implication is that any realistic modelling of the impact of IOD activity on EICC should account for a proper level of turbulence. The coarse grid of ORAS4, visibly precluding a significant development of ocean turbulence in the BoB, is probably responsible for the excessive statistical relationship between IOD activity and EICC variability. In contrast, the eddying capacity of ORCA12 (Benshila et al., 2014) allows other forcing mechanisms (typically mesoscale eddies) to also modulate the EICC at non-seasonal timescales, which act independently from IOD activity. Forcing from local wind anomalies, and/or from remote wind anomalies not related to IOD (such as the Madden-Julian Oscillation, described by Zhang (2005)) must also be considered to understand EICC non-seasonal variability. Recent numerical studies indeed suggest a marked influence of Madden-Julian Oscillation on the intra-seasonal variability of the EICC (Suresh et al., 2013).

Acknowledgements

This work was performed with the support of the Ministry of Earth Sciences, Government of India through INCOIS, Hyderabad. The authors thank all the project staff for their efforts in collecting XBT/XCTD data. Sincere thanks to Nisha Kurian, Manu Thambi and Glen Fernandes for processing part of the *in situ* data. We also thank IRD for financial support of FD and FP. We acknowledge financial support from a TOSCA project from CNES, the

French Space Agency. The Indo-French Cell for Water Sciences (Indian Institute of Science, Bangalore, India) hosted us during the completion of this study. We are thankful to the SODA and ORAS4 projects for making their products freely available.

References

- Akhil, V. P., Durand, F., Lengaigne, M., Vialard, J., Keerthi, M. G., Gopalakrishna, V. V., Deltel, C., Papa, F., de Boyer Montégut, C., 2014. A modeling study of the processes of surface salinity seasonal cycle in the Bay of Bengal. *J. Geophys. Res.*, 119, 3926–3947, doi:10.1002/2013JC009632.
- Akhil, V. P., Lengaigne, M., Vialard, J., Durand, F., Keerthi, M. G., Chaitanya, A. V. S., Papa, F., de Boyer Montégut, C., 2016. A modelling study of processes controlling the Bay of Bengal sea surface salinity interannual variability. *J. Geophys. Res.*, 121, doi:10.1002/2016JC011662.
- Aparna, S.G., McCreary, J.P., Shankar, D., Vinayachandran, P.N., 2012. Signatures of Indian Ocean Dipole and El Niño–Southern Oscillation events in sea level variations in the Bay of Bengal. *J. Geophys. Res.* 117, 1–13, doi:10.1029/2012JC008055
- Bailey, R., Gronell, A., Phillips, H., Tanner, E., Meyers, G., 1994. Quality Control Cookbook for XBT Data. Report 221. CSIRO, Marine Laboratories, CSIRO Australia.
- Balmaseda, M.A., Mogensen, K., Weaver, A.T., 2013. Evaluation of the ECMWF ocean reanalysis system ORAS4. *Q. J. R. Meteorol. Soc.* 139, 1132–1161. doi:10.1002/qj.2063
- Benshila, R., Durand, F., Masson, S., Bourdalle-Badie, R., de Boyer Montégut, C., Papa, F., Madec, G., 2014. The upper Bay of Bengal salinity structure in a high-resolution model. *Ocean Modeling* 74, 36–52, doi:10.1016/j.ocemod.2013.12.001.
- Boyer, T.P., Antonov, J. I., Baranova, O. K., Coleman, C., Garcia, H. E., Grodsky, A., Johnson, D. R., Locarnini, R. A., Mishonov, A., O'Brien, T. D., Paver, C. R., Reagan, J. R., Seidov, D., Smolyar, I. V., Zweng, M. M., 2013. World Ocean Database 2013. NOAA Atlas NESDIS 72, S. Levitus, Ed., A. Mishonov, Technical Ed.; Silver Spring, MD, 209 pp.
- Carton, J.A., Giese, B.S., 2008. A Reanalysis of Ocean Climate Using Simple Ocean Data Assimilation (SODA). *Mon. Weather Rev.* 136, 2999–3017, doi:10.1175/2007MWR1978.1
- Chaitanya, V. S., Lengaigne, M., Vialard, J., Gopalakrishna, V.V., Durand, F., KranthiKumar, C., Amritash, S., Suneel, V., Papa, F., Ravichandran, M., 2014. Salinity Measurements Collected by Fishermen Reveal a “River in the Sea” Flowing Along the Eastern Coast of India, *Bull. Am. Meteorol. Soc.*, 95, 1897–1908, doi:10.1175/BAMS-D-12-00243.1
- Chaitanya, A. V. S., Durand, F., Mathew, S., Gopalakrishna, V. V., Papa, F., Lengaigne, M., Vialard, J., Krantikumar, C., Venkatesan, R., 2015. Observed year-to-year sea surface salinity variability in the Bay of Bengal during the period 2009–2014, *Ocean Dyn.*, doi:10.1007/s10236-014-0802-x.

- Chao, Y., Gangopadhyay, A., Bryan, F.O., Holland, W.R., 1996. Modeling the Gulf Stream System: How far from reality? *Geophys. Res. Lett.* 23, 3155–3158, doi:10.1029/96GL03003
- Chatterjee, A., Shankar, D., Shenoi, S.S.C., Reddy, G. V., Michael, G.S., Ravichandran, M., Gopalkrishna, V. V., Rama Rao, E.P., Udaya Bhaskar, T.V.S., Sanjeevan, V.N., 2012. A new atlas of temperature and salinity for the North Indian Ocean. *J. Earth Syst. Sci.* 121, 559–593, doi:10.1007/s12040-012-0191-9
- Chen, G., Wang, D., Hou, Y., 2012. The features and interannual variability mechanism of mesoscale eddies in the Bay of Bengal. *Cont. Shelf Res.* 47, 178–185, doi:10.1016/j.csr.2012.07.011
- Cheng, X., Xie, S.-P., McCreary, J.P., Qi, Y., Du, Y., 2013. Intraseasonal variability of sea surface height in the Bay of Bengal. *J. Geophys. Res. Ocean.* 118, 816–830, doi:10.1002/jgrc.20075
- Chowdary, J.S., Srinivas, G., Fousiya, T.S., Parekh, A., Gnanaseelan, C., Seo, H., MacKinnon, J. A., 2016. Representation of Bay of Bengal upper-ocean salinity in general circulation models. *Oceanography* 29(2), 38–49, doi:10.5670/oceanog.2016.37.
- Currie, J. C., Lengaigne, M., Vialard, J., Kaplan, D. M., Aumont, O., Naqvi, S. W. A., and Maury, O., 2013. Indian Ocean Dipole and El Niño/Southern Oscillation impacts on regional chlorophyll anomalies in the Indian Ocean, *Biogeosciences*, 10, 6677–6698, doi:10.5194/bg-10-6677-2013.
- Dee, D. P., Uppala, S. M., Simmons, A. J., Berrisford, P., Poli, P., Kobayashi, S., Andrae, U., Balmaseda, M. A., Balsamo, G., Bauer, P., Bechtold, P., Beljaars, A. C. M., van de Berg, L., Bidlot, J., Bormann, N., Delsol, C., Dragani, R., Fuentes, M., Geer, A. J., Haimberger, L., Healy, S. B., Hersbach, H., Hólm, E. V., Isaksen, L., Kållberg, P., Köhler, M., Matricardi, M., McNally, A. P., Monge-Sanz, B. M., Morcrette, J.-J., Park, B.-K., Peubey, C., de Rosnay, P., Tavolato, C., Thépaut, J.-N., and Vitart, F., 2011. The ERA-Interim reanalysis: configuration and performance of the data assimilation system. *Q.J.R. Meteorol. Soc.*, 137: 553–597, doi:10.1002/qj.828.
- Durand, F., Shankar, D., de Boyer Montégut, C., Shenoi, S.S.C., Blanke, B., Madec, G., 2007. Modeling the barrier-layer formation in the southeastern Arabian Sea. *J. Clim.* 20, 2109–2120, doi:10.1175/JCLI4112.1
- Durand, F., Shankar, D., Birol, F., Shenoi, S.S.C., 2009. Spatiotemporal structure of the East India Coastal Current from satellite altimetry. *J. Geophys. Res. Ocean.* 114, 1–18, doi:10.1029/2008JC004807
- Han, W., Webster, P.J., 2002. Forcing Mechanisms of Sea Level Interannual Variability in the Bay of Bengal. *J. Phys. Oceanogr.* 32, 216–239, doi:10.1175/1520-0485(2002)032<0216:FMOSLI>2.0.CO;2
- Hanawa, K., Rual, P., Bailey, R., Sy, A., Szabados, M., 1995. A new depth-time equation for Sippican or TSK T-7, T-6, and T-4 expendable bathythermographs (XBT). *Deep-Sea Res.* I 42, 1423–1451, doi:10.1016/0967-0637(95)97154-Z.
- Hewitt, H. T., Roberts, M. J., Hyder, P., Graham, T., Rae, J., Belcher, S. E., Bourdallé-Badie,

- R., Copsey, D., Coward, A., Guiavarch, C., Harris, C., Hill, R., Hirschi, J. J. M., Madec, G., Mizielinski, M. S., Neinger, E., New, A. L., Rioual, J. C., Sinha, B., Storkey, D., Shelly, A., Thorpe, L., and Wood, R. A., 2016. The impact of resolving the Rossby radius at mid-latitudes in the ocean: results from a high-resolution version of the Met Office GC2 coupled model. *Geosci. Model Dev*, 9, 3655-3670, doi:10.5194/gmd-9-3655-2016.
- Jackett, D.R., McDougall, T. J., Feistel, R., Wright, D. G., Griffies, S., M., 2006. Algorithms for density, potential temperature, conservative temperature and the freezing temperature of seawater. *Journal of Atmospheric and Oceanic Technology*, 23, 1709–1728, doi:0.1175/JTECH1946.1
- Jensen, T.G., 2001. Arabian Sea and Bay of Bengal exchange of salt and tracers in an ocean model. *Geophysical Research Letters*, 28, 3967–3970, doi:10.1029/2001GL013422.
- Jensen, T.G., 2007. Wind-driven response of the northern Indian Ocean to climate extremes. *J. Clim.* 20, 2978–2993, doi:10.1175/JCLI4150.1
- Jensen, T.G., Wijesekera, H. W., Nyadjro, E. S., Thoppil, P. G., Shriver, J. F., Sandeep, K. K., Pant, V., 2016. Modeling salinity exchanges between the equatorial Indian Ocean and the Bay of Bengal. *Oceanography* 29(2), 92–101, doi:10.5670/oceanog.2016.42.
- Laurindo, L.C., Mariano, M.J., Lumpkin, R., 2017. An improved near-surface velocity climatology for the global ocean from drifter observations. *Deep-Sea Research Part I*, volume 124, 73-92 doi:10.1016/j.dsr.2017.04.009.
- Lellouche, J.M., Le Galloudec, O., Regnier, C., Levier, B., Greiner E., Drevillon, M., 2016. CMEMS Quality Information Document For Global Sea Physical Analysis and Forecasting Product, GLOBAL_ANALYSIS_FORECAST_PHY_001_024, available on <http://cmems-resources.cls.fr/documents/QUID/CMEMS-GLO-QUID-001-024.pdf>
- Locarnini, R. A., Mishonov, A. V, Antonov, J. I., Boyer, T. P., Garcia, H. E., Baranova, O. K., Zweng, M. M., Paver, C. R., Reagan, J. R., Johnson, D. R., Hamilton, M., Seidov, D., 2013. *World Ocean Atlas 2013, Volume 1: Temperature*. S. Levitus, Ed., A. Mishonov Technical Ed.; NOAA Atlas NESDIS 73 , Silver Spring, MD, 40 pp.
- Madec, G., 2008. NEMO reference manual, ocean dynamics component. Note du pôle de modélisation, IPSL, France No. 27 ISSN No. 1288–1619.
- Madhupratap M, Gauns M, Ramaiah N, Kumar S P, Muraleedharan, P. M., 2003. Biogeochemistry of the Bay of Bengal: Physical, chemical and primary productivity characteristics of the central and western Bay of Bengal during summer monsoon 2001. *Deep-Sea Res. Part II*, 50, 881–896, doi:10.1016/S0967-0645(02)00611-2
- McCreary, J. P., Kundu, P. K., Molinari, R. L., 1993. A numerical investigation of dynamics, thermodynamics and mixed-layer processes in the Indian Ocean. *Prog. Oceanogr.* 31, 181–244, doi:10.1016/0079-6611(93)90002-U.
- McCreary, J.P., Han, W., Shankar, D., Shetye, S.R., 1996. Dynamics of the East India Coastal Current: 2. Numerical solutions. *J. Geophys. Res. Ocean.* 101, 13993–14010. doi:10.1029/96JC00560.

- Mukherjee, A., Shankar, D., Fernando, V., Amol, P., Aparna, S.G., Fernandes, R., Michael, G.S., Khalap, S.T., Satelkar, N.P., Agarvadekar, Y., Gaonkar, M.G., Tari, A.P., Kankonkar, A., Vernekar, S., 2014. Observed seasonal and intraseasonal variability of the east india coastal current on the continental slope. *J. Earth Syst. Sci.* 123, 1197–1232, doi:10.1007/s12040-014-0471-7.
- Pant, V., Girishkumar, M. S, Udaya Bhaskar, T. V. S., Ravichandran, M., Papa, F., Thangaprakash, V.P., 2015. Observed interannual variability of near-surface salinity in the Bay of Bengal, *J. Geophys. Res. Oceans*, 120, 3315–3329, doi:10.1002/2014JC010340.
- Potemra, J.T., Luther, M.E., O'Brien, J.J., 1991. The seasonal circulation of the upper ocean in the Bay of Bengal. *J. Geophys. Res.* 96, 12667–12683, doi:10.1029/91JC01045.
- Rao, R.R., Girish Kumar, M.S., Ravichandran, M., Rao, A.R., Gopalakrishna, V. V., Thadathil, P., 2010. Interannual variability of Kelvin wave propagation in the wave guides of the equatorial Indian Ocean, the coastal Bay of Bengal and the southeastern Arabian Sea during 1993-2006. *Deep. Res. Part I Oceanogr. Res. Pap.* 57, 1–13. doi:10.1016/j.dsr.2009.10.008.
- Rao, S.A., Behera, S.K., Masumoto, Y., Yamagata, T., 2002. Interannual subsurface variability in the tropical Indian Ocean with a special emphasis on the Indian Ocean Dipole. *Deep Sea Res. Part II Top. Stud. Oceanogr.* 49, 1549–1572. doi:10.1016/S0967-0645(01)00158-8.
- Sudre, J., Maes, C., Garçon, V., 2013. On the global estimates of geostrophic and Ekman surface currents. *Limnol. Oceanogr.: Fluids Environ.*, 3, 1–20, doi:10.1215/21573689-2071927.
- Saji, N.H., Goswami, B.N., Vinayachandran, P.N., Yamagata, T., 1999. A dipole mode in the tropical Indian Ocean. *Nature* 401, 360–363, doi:10.1038/43854.
- Sanilkumar, K. V., Kuruvilla, T. V., Jogendranath, D., Rao, R.R., 1997. Observations of the Western Boundary Current of the Bay of Bengal from a hydrographic survey during March 1993. *Deep. Res. Part I*, 44, 135–145. doi:10.1016/S0967-0637(96)00036-2.
- Schott, F.A., McCreary, J.P., 2001. The monsoon circulation of the Indian Ocean. *Prog. Oceanogr.* 51, 1–123, doi:10.1016/S0079-6611(01)00083-0.
- Sérazin, G., Penduff, T., Grégorio, S., Barnier, B., Molines, J.-M., Terray, L., 2015. Intrinsic Variability of Sea Level from Global Ocean Simulations: Spatiotemporal Scales. *J. Clim.* 28, 4279–4292, doi:10.1175/JCLI-D-14-00554.1.
- Shankar, D., McCreary, J.P., Han, W., Shetye, S.R., 1996. Dynamics of the East India Coastal Current I. Analytic solutions forced by interior Ekman pumping and local alongshore winds. *J. Geophys. Res.* 101, 13993–14010, doi:10.1029/96JC00560.
- Shankar, D., Vinayachandran, P.N., Unnikrishnan, A.S., 2002. The monsoon currents in the north Indian Ocean. *Prog. Oceanogr.* 52, 63–120, doi:10.1016/S0079-6611(02)00024-1.
- Shenoi, S.S.C., Shankar, D., Shetye, S.R., 1999. On the sea surface temperature high in the Lakshadweep Sea before the onset of the southwest monsoon. *J. Geophys. Res. Ocean.* 104, 15703–15712, doi:10.1029/1998JC900080.

- Shenoi, S.S.C., Shankar, D., Shetye, S.R., 2002. Differences in heat budgets of the near-surface Arabian Sea and Bay of Bengal: Implications for the summer monsoon. *J. Geophys. Res.* 107, 1–14, doi:10.1029/2000JC000679.
- Shetye, S.R., Shenoi, S.S.C., Gouveia, A.D., Michael, G.S., Sundar, D., Nampoothiri, G., 1991. Wind-driven coastal upwelling along the western boundary of the Bay of Bengal during the southwest monsoon. *Cont. Shelf Res.* 11, 1397–1408, doi:10.1016/0278-4343(91)90042-5.
- Shetye, S.R., Gouveia, A.D., Shenoi, S.S.C., Sundar, D., Michael, G.S., Nampoothiri, G., 1993. The western boundary current of the seasonal subtropical gyre in the Bay of Bengal. *J. Geophys. Res. Ocean.* 98, 945–954, doi:10.1029/92JC02070.
- Shetye, S.R., Shankar, D., Gouveia, A. D., Shenoi, S.S.C., Vinayachandran, P.N., Sundar, D., Michael, G.S., Nampoothiri, G., 1996. Hydrography and circulation in the western Bay of Bengal during the northeast monsoon. *J. Geophys. Res.* 101, 14011, doi:10.1029/95JC03307.
- Srinivas K, Kumar P K D, Revichandran, C., 2005. ENSO signature in the sea level along the coastline of the Indian subcontinent. *Indian J. Mar. Sci.* 34 225–236.
- Sudre, J., Maes, C., Garçon, V., 2013. On the global estimates of geostrophic and Ekman surface currents. *Limnology and Oceanography: Fluids and Environments*, 3, 10.1215/21573689-2071927.
- Suresh, I., Vialard, J., Lengaigne, M., Han, W., McCreary, J. P., Durand, F., Muraleedharan, P. M., 2013. Origins of wind-driven intraseasonal sea level variations in the North Indian Ocean coastal waveguide, *Geophys. Res. Lett.*, 40, 5740–5744, doi:10.1002/2013GL058312.
- Taft, B. A., Kessler, W. S., 1991. Variations of zonal currents in the central tropical Pacific during 1970 to 1987: Sea level and dynamic height measurements, *J. Geophys. Res.*, 96(C7), 12599–12618, doi:10.1029/91JC00781.
- Thompson, B., Gnanaseelan, C., Salvekar, P.S., 2006. Variability in the Indian Ocean circulation and salinity and its impact on SST anomalies during dipole events. *J. Mar. Res.* 64, 853–880, doi:10.1357/002224006779698350.
- Umlauf, L., Burchard, H., 2003. A generic length-scale equation for geophysical turbulence models, *J. Mar. Res.*, 61, 235–265, doi:10.1357/002224003322005087
- Vinayachandran, P.N., Shetye, S.R., Sengupta, D., Gadgil, S., 1996. Forcing mechanisms of the Bay of Bengal Circulation. *Curr. Sci.* 71, 753–763.
- Vinayachandran, P.N., Masumoto, Y., Mikawa, T., Yamagata, T., 1999. Intrusion of the southwest monsoon current into the Bay of Bengal. *J. Geophys. Res.* 104, 11077–11085. doi:10.1029/1999JC900035.
- Webster, P.J., Moore, A. M., Loschnigg, J.P., Leben, R.R., 1999. Coupled ocean-atmosphere dynamics in the Indian Ocean during 1997-98. *Nature*, 401, 356–360, doi:10.1038/43848.
- Wijesekera, H. W., Jensen, T. G., Jarosz, E., Teague, W. J., Metzger, E. J., Wang, D. W.,

- Jinadasa, S. U. P., Arulananthan, K., Centurioni, L. R. Fernando, H. J. S., 2015. Southern Bay of Bengal currents and salinity intrusions during the northeast monsoon, *J. Geophys. Res. Oceans*, 120, 6897–6913, doi:10.1002/2015JC010744.
- Yu L, O'Brien, J. J., Yang, J., 1991. On the remote forcing of the circulation in the Bay of Bengal; *J. Geophys. Res.* 96 20,449–20,454, doi: 10.1029/91JC02424
- Zhang, C., 2005. Madden-Julian oscillation, *Rev. Geophys.*, 43, RG2003, doi:10.1029/2004RG000158.
- Zweng, M.M, Reagan, J. R., Antonov, J. I., Locarnini, R. A., Mishonov, A. V., Boyer, T. P., Garcia, H. E., Baranova, O. K., Johnson, D. R., Seidov, D., Biddle, M. M., 2013. *World Ocean Atlas 2013, Volume 2: Salinity*. S. Levitus, Ed., A. Mishonov Technical Ed.; NOAA Atlas NESDIS 74 , Silver Spring, MD, 39 pp.